Tracking Autonomic Balance Using Open and Closed Loop Models of the Arterial Baroreflex

by

Jonathan Birjiniuk

B.S., Massachusetts Institute of Technology (2015)

Submitted to the
Department of Electrical Engineering and Computer Science
In partial fulfillment of the requirements for the degree of

Master of Engineering in Electrical Engineering and Computer Science

at the

MASSACHUSETTS INSTITUTE OF TECHNOLOGY

June 2017

Author . . . . . .
Department of Electrical Engineering and Computer Science
May 26th 2017

Certified by . . . . . .
Thomas Heldt
W.M. Keck Career Development Professor
Thesis Supervisor

Accepted by . . . . . .
Christopher J. Terman
Chairman, Master of Engineering Thesis Committee

Tracking Autonomic Balance Using Open and Closed Loop Models of the Arterial Baroreflex

by

Jonathan Birjiniuk

B.S., Massachusetts Institute of Technology (2015)

Submitted to the
Department of Electrical Engineering and Computer Science
on May 26, 2017, in partial fulfillment of the requirements for the degree of
Master of Engineering in Electrical Engineering and Computer Science

Abstract

The arterial baroreceptor reflex is the major blood pressure control loop mediated by the autonomic nervous system (ANS). It supports arterial blood pressure homeostasis by dynamically adjusting heart rate, vascular resistance, venous tone, and cardiac contractility. Accurate quantitative models of the baroreflex would provide physiological insight, and could allow for real-time tracking of ANS activity in clinical settings. Prior work has concentrated on modeling the baroreflex nonparametrically with linear transfer functions, or parametrically as an autoregressive moving average model. In this work, we formulate beat-to-beat, open and closed loop models of the heart rate arc of the baroreflex. Model structure and parameterization are explicitly based on prior physiological insights of the response dynamics of the sympathetic and parasympathetic branches of the ANS. We analyze the models' ability to track changes in autonomic balance using data from a dual pharmacological blockade and postural study. Our results show that the open loop model parameters faithfully track changes in autonomic balance resulting from changing posture and autonomic blockade, whereas the closed loop model parameters do not. Sensitivity analyses are conducted on the open-loop model parameter estimation, which proves to be robust in the presence of varying levels of noise. Overall, the contributions of this thesis further the goal of obtaining real-time information about the ANS.

Thesis Supervisor: Thomas Heldt
Title: W.M. Keck Career Development Professor in Biomedical Engineering

Acknowledgements

First, I would like to acknowledge Professor Thomas Heldt, who for the past two years has been my advisor, my mentor, and my teacher. My project would not have been successful without your focus and deep insight. Your devotion to your students is self-evident, and you have made me a better engineer.

To the gentlemen of E25-324 proper: Rohan, James, Freddie, and Imad, thank you for the all the humor and support that make coming into a lab everyday an enjoyable experience. I would especially like to thank James, who set up the cluster on which most of the computation of this project was executed.

To Mom and Dad, you two have always been and always will be my greatest influence. I know I can always find love and support from you two even in the most difficult of times. To Alona, thank you for your constant reminders to work on my thesis; I certainly needed them during my many periods of procrastination. To Joav, thank you for not only being my best friend, but for always finding time in your hectic life to answer my often simple medical questions. I hope you will cherish these last two years of medical school as much as I will cherish these next two years where I will technically have more degrees than you.

Finally, I would like to acknowledge the original pioneers, the mathematicians who have made this work possible: Isaac Newton, Carl Friedrich Gauss, Joseph Fourier, Pierre-Simon Laplace, and Witold Hurewicz.

Contents

1 Introduction **13**
1.1 Motivation 13
1.2 Prior Work 14
1.3 Approach. 14
1.4 Thesis Outline 15

2 Background **17**
2.1 Cardiovascular Physiology. 17
2.1.1 Cardiovascular Mechanics 18
2.1.2 Cardiovascular Electrophysiology 21
2.1.3 Hemodynamics. 23
2.2 Cardiovascular Control. 24
2.2.1 Autonomic Nervous System 25
2.2.2 Arterial Baroreflex 26
2.3 Heart Rate Variability 28

3 Open-Loop Modeling of Baroreflex and Baroreflex Sensitivity **31**
3.1 Open-loop Response and Baroreflex Sensitivity. . . . 31
3.2 Black-box Open-loop Model 33
3.3 Measuring Baroreflex Sensitivity 34
3.4 Parametric Open-loop Model 36

4 Open-loop Model Analysis **39**
4.1 Experimental Data Set 39
4.2 Transfer Function Analysis 41

4.2.1 Results 41
4.3 Open-loop Parameter Estimation 45
4.3.1 Results 52
4.3.2 Discussion 57

5 Closed-loop Modeling of Baroreflex 61
5.1 Closed-loop Framework 62
5.2 Parameterization 63
5.2.1 Baroreceptors (sensor) 63
5.2.2 Autonomous Nervous System (controller) . . 64
5.2.3 Cardiovascular System (plant). 64
5.2.4 Full Model 65
5.3 Noise 65
5.3.1 Sources 66
5.3.2 Error Compensation 66

6 Closed-loop Model Analysis 69
6.1 Closed-loop Parameter Estimation 69
6.2 Results 71
6.3 Discussion 75

7 Sensitivity Analysis 77
7.1 Methods 77
7.2 Results 79

8 Conclusions 85
8.1 Contributions 85
8.2 Future Work 86

A Transfer Function Analysis Methodology 89

Bibliography 93

List of Figures

2.1 Sketch of the heart displaying the four chambers, the four valves, and the major vessels. Taken from [1]. 18
2.2 Traces of the aortic, left atrial, and left ventricular pressures over the duration of one cardiac cycle. Taken from [2]. 20
2.3 Diagram of the heart's electrical conduction system. Taken from [3]. . 22
2.4 Lead II ECG with standard morphological labels (left). The P, QRS complex, and T wave, correspond to atrial depolarization, ventricular depolarization, and ventricular repolarization respectively . Sample measurement of an R-R interval in a lead II ECG trace (right). Both figures taken from [5]. 23
2.5 Sketch of the ANS's neurochemical pathways. ACh, NE, Epi, and D, represent the acetylcholine, norepinephrine, epinephrine, and dopamine neurotransmitters, respectively. M, N, α, and β, represent the muscarinic, nicotinic, alpha, and beta receptors respectively. Taken from [6]. 26
2.6 Sketch of the baroreceptors and their efferent pathways to the brain. Taken from [6]. 27
3.1 Illustrative cartoon of the sigmoidal response in RRI to incremental changes in systolic blood pressure (SBP). The purple dot indicates the operating point of this specific baroreflex curve, which is set to a SBP of 90 mmHg and an RRI of 825 ms. The blue line is the tangent line of the sigmoid at the operating point. Note that as distance from the operating point increases, the slope of the sigmoid decreases. 32
3.2 Open-loop, black-box model for baroreflex. 34
3.3 The canine's parasympathetic impulse response (top), and sympathetic impulse response (bottom) [13]. Top Right: ABP→HR transfer function in humans [14]. Bottom Right: Decoupling of parasympathetic and sympathetic effects on the ABP→HR transfer function [12]. Full figure taken from [12]. 37
3.4 Overall open-loop parametric model for baroreflex. The diagram on the

left displays the two sub-systems, one for each branch of the autonomic nervous system. The diagram on the right displays the parameterizations of the two branches. 38
4.1 BRS values from supine (SUC) to standing (STC) without pharmacological intervention. 42
4.2 BRS values from supine and no pharmacological blockade (SUC), and supine after application of atropine (SUA). 43
4.3 BRS values from standing and no pharmacological blockade state (STC), and standing with application of propranolol (STP). 44
4.4 SBP time series comparison plot for 08STC (top) and the estimated model parameters over time (bottom). The RMSE between the true and estimated heart rate time series for this recording is 4.0 bpm. The units of K_p, K_s, and β are $\frac{bpm}{mmHg}$, $\frac{bpm}{(beat)*(mmHg)}$, and $\frac{1}{beat}$ respectively. 48
4.5 Estimated and actual HR time series for 02STC (top), and actual HR and SBP time series for 02STC (bottom). Note that 02STC coheres well with our model assumptions as the SBP and true HR signals are almost completely 180° out of phase with each other. This manifests in close estimation of the HR time series. 50
4.6 Estimated and actual HR time series for 01SUC (top), and actual HR and SBP time series for 01SUC (bottom). 01SUC does not cohere well with our model assumptions as the SBP and true HR signals are inconsistently out of phase with each other. This manifests in poor estimation of the HR time series. 51
4.7 Plot of PSR in the SUC and STC states for twelve subjects. Subject 12 is excluded, as there were no windows that fit the acceptance criterion. . 52
4.8 Comparison of PSR between the STC and STP recordings (top), and comparison of K_s between the STC and STP recordings (bottom). Figure shows means (bars) and standard deviations (error bars). 54
4.9 Comparison of PSR between the SUC and SUA recordings (top), and comparison of K_p between the SUC and SUA recordings (bottom). Figure shows means (bars) and standard deviations (error bars). 55
4.10 Graphical comparison of decreasing RMSE as taps increase. 14STC is one of the five missing records, hence its exclusion from this graph. 56
5.1 Canonical negative feedback control system. 62
5.2 Block diagram of the heart rate baroreflex feedback loop. 63
5.3 Fully parameterized closed loop model of baroreflex. 65
5.4 Closed loop model in the presence of noise. Hat notation implies estimate, i.e. $\widehat{\mathrm{dHR}}$ is an estimate of the true value of dHR, and $\widehat{\mathrm{dSBP}}$ is an estimate of the true value of dSBP. 65
5.5 Updated control loop with error compensation. 67

6.1 Plot of PSR in the SUC and STC states for thirteen subjects computed given CLM model (top) and CLECM model (bottom). 73
6.2 For CLM, comparison of PSR between the STC and STP recordings (left), and comparison of K_s between the SUC and SUA recordings (right). . 74
6.3 For CLM, comparison of PSR between the SUC and SUA recordings(left), and comparison of K_p between the SUC and SUA recordings (right). . 74
6.4 For the CLECM, comparison of PSR between the STC and STP recordings (left), and comparison of K_s between the SUC and SUA recordings (right). 74
6.5 For the CLECM, comparison of PSR between the SUC and SUA recordings (left), and comparison of K_p between the SUC and SUA recordings (right). 75
7.1 Changes in PSR from SUC to STC for each perturbation scheme. The "No Noise" scheme is the original set of estimates. Population mean is represented by the subject "pop." 80
7.2 Changes in K_s from STC to STP for each perturbation scheme (top). Changes in K_p from SUC to SUA for each perturbation scheme (bottom). The subject "pop" represents population mean. 82
7.3 Estimated K_s in STC state for each perturbation scheme (top). Estimated K_p in SUC state for each perturbation scheme (bottom). The subject "pop" represents population mean. 83

Chapter 1

Introduction

In this chapter we motivate the objective of this thesis and briefly review some prior work related to the objective. We then summarize our approach, and outline the structure of the thesis.

1.1 Motivation

The arterial baroreceptor reflex (baroreflex) is the major blood pressure control loop mediated by the autonomic nervous system (ANS). Blood pressure control is vital for maintaining adequate perfusion of the brain and other organs in the body across varying physiological states. An abnormal or impaired ANS, known as dysautonomia, can be caused by conditions such as traumatic brain injury, stroke, and amyloidosis, and may lead to a wide array of conditions including dizziness, orthostatic hypotension, and rapid heart rate. Real-time tracking of aggregate ANS activity and autonomic balance (the relative strengths of the two branches of the ANS) could be useful in clinical settings by providing physicians with information about the trajectory of a patient's ANS activity.

This work attempts to develop methods for real-time quantification of autonomic balance using different models of the baroreflex.

1.2 Prior Work

In the literature, autonomic balance is often estimated either through the examination of heart rate variability, or the analysis of models of the baroreflex relating arterial blood pressure, heart rate, and respiration. Heart rate variability based methods of determining autonomic balance are generally inaccurate due to the difficulty in disambiguating the effects of the sympathetic and parasympathetic actions of the ANS on heart rate from heart rate data alone. In contrast, the baroreflex modeling work has been better able to capture the dynamics of autonomic balance, but the model structures do not lend themselves to easy interpretability. In particular, the baroreflex is commonly modeled nonparametrically with linear transfer functions or parametrically as an autoregressive moving average model. Physiological understanding typically plays a role in the interpretation of these models, but less in their formulation.

1.3 Approach

In this work we first modeled the baroreflex using low order, open and closed-loop models. We then estimated the parameters for each models across a variety of subjects and experimental conditions using data from a dual pharmacological blockade and postural study (N=14 subjects). Afterwards, we estimated autonomic balance in the subjects based on parameters extracted from our open and closed-loop models. Our approach differs from prior modeling of the baroreflex as we impose model structures

and parameterizations explicitly based on prior physiological insights of the response dynamics of the two branches of the ANS.

1.4 Thesis Outline

The remainder of this thesis is organized as follows. In Chapter 2 we introduce cardiovascular control physiology and review the heart rate variability literature. We then develop both an open loop model of the baroreflex and measures for quantifying baroreflex sensitivity in Chapter 3. In Chapter 4 we formulate a parameter estimation method for the open-loop model. We subsequently apply this method to a dual pharmacological blockade and postural study, estimating open-loop model parameters and demonstrate the model's ability to faithfully track autonomic balance. A closed loop model of the baroreflex is developed in Chapter 5 and parameter estimation process similar to that in Chapter 4 is performed on the models in Chapter 6. In Chapter 7, we probe the sensitivity of the open loop model and parameter estimation to noise. We finally conclude the thesis with a brief summary of our results and further work to be done in the field in Chapter 8.

Chapter 2

Background

Modeling the arterial baroreceptor reflex (baroreflex) is a difficult task that requires an appreciation for many facets of cardiovascular and neural physiology. We begin this chapter by introducing the mechanics and electrophysiology of the cardiovascular system. We then present the autonomic nervous system and its relationship to cardiac control, culminating in a description of the arterial baroreflex. Finally, we review a domain of literature that probes fluctuations in heart rate and attempts to measure sympathovagal balance.

2.1 Cardiovascular Physiology

The primary function of the cardiovascular system is to keep the central nervous system perfused with oxygenated blood. It realizes this function through rhythmic pumping of the heart, which facilitates the circulation of oxygenated and deoxygenated blood throughout the body. This rhythmic pumping also serves to transport nutrients to organs

and tissue throughout the body, and carry away carbon dioxide and other waste products for elimination.

2.1.1 Cardiovascular Mechanics

The heart is a muscular pump composed of four chambers: the right atrium, the right ventricle, the left atrium and the left ventricle (Figure 2.1). The atria are the upper chambers of the heart. They receive blood from their respective veins and empty into the ventricles. The ventricles are the lower chambers of the heart. They pump blood into their respective arteries. At the ventriculo-arterial junctions of each chamber is a mechanical valve that prevents reverse flow into the chamber.

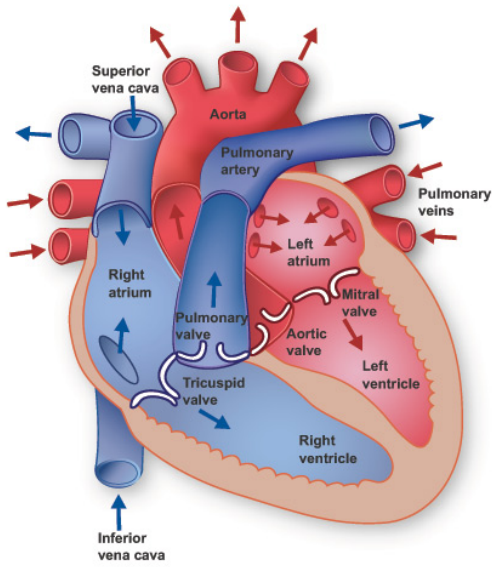

Figure 2.1: Sketch of the heart displaying the four chambers, the four valves, and the major vessels. Taken from [1].

In addition to the vertical differentiation of the heart chambers, heart function is lateralized. During each heartbeat, the right side of the heart receives deoxygenated blood from the body via the vena cavae and pumps that blood to the lungs via the pulmonary

artery. Simultaneously, the left side of the heart receives oxygenated blood from the lungs via the pulmonary vein, and pumps that blood out to the body via the aorta. The pumping mechanisms are pressure gradients formed by the rhythmic contraction and relaxation of the myocardium (cardiac muscle). The sequence of events that causes the beat-to-beat pumping of the heart is defined as the cardiac cycle, and is divided into five stages explained below and illustrated in Figure 2.2.

Atrial Systole: This is the first stage of the cardiac cycle, during which the atria contract, raising blood pressure in the atria. Throughout this stage, the tricuspid and mitral valves are open while the pulmonary and aortic valves are closed.

Isovolumetric Contraction: Following atrial systole all of the heart valves shut and the ventricles contract, increasing blood pressure in the ventricles while maintaining a constant volume.

Ventricular Ejection: When the pressure in the left ventricle exceeds the pressure in the aorta, the aortic valve opens, and oxygenated blood is ejected to the rest of the body. In parallel, when the pressure in the right ventricle exceeds the pressure in the pulmonary artery, the pulmonic valve opens and deoxygenated blood is ejected into the lungs. Systolic arterial blood pressure (SBP), which is the peak blood pressure during the cardiac cycle, occurs during this stage.

Isovolumetric Relaxation: Towards the end of ejection the ventricular pressure drops. Once the left ventricular pressure falls below the aortic pressure, the aortic valve shuts, and once the right ventricular pressure falls below the pulmonary arterial pressure, the pulmonary valve closes. The closing of these valves commences isovolumetric relaxation, with the ventricular pressure continuing to decrease while volume remains constant.

Ventricular Filling: In this stage, blood from the atria fill into the ventricles, which is initiated by the opening of the tricuspid and mitral valves. This occurs when the ventricular pressures drop below the atrial pressures.

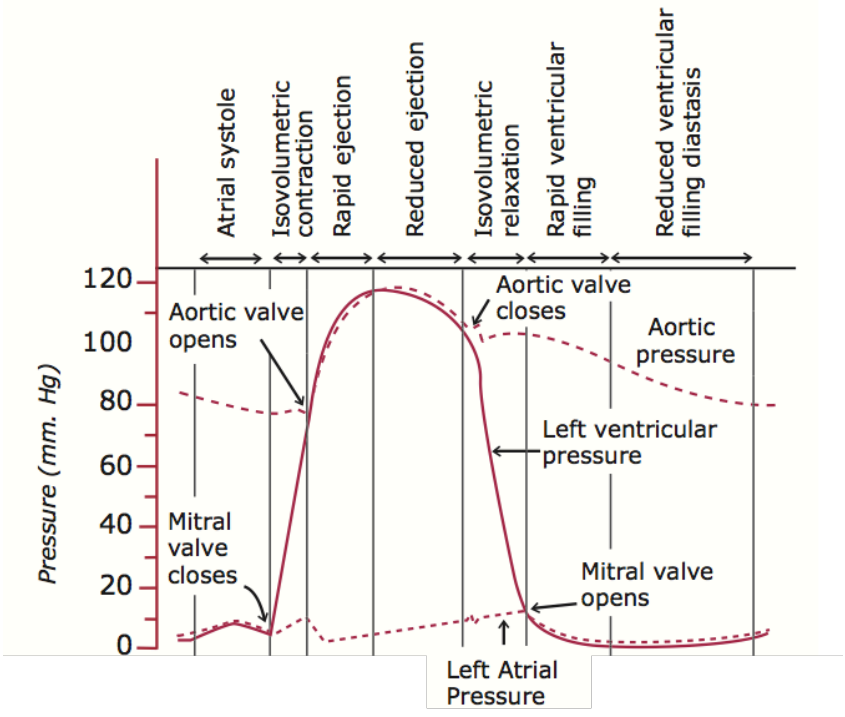

Figure 2.2: Traces of the aortic, left atrial, and left ventricular pressures over the duration of one cardiac cycle. Taken from [2].

As blood leaves the left ventricle it encounters the *systemic vasculature*. These vessels include arteries, veins and capillaries, and resist the flow of blood. The net resistance to

blood flow provided by the systemic vasculature is defined as the total peripheral resistance (TPR), which is measured in *Peripheral Resistance Units (PRU)*, where $1\,\boldsymbol{PRU} = 1\,\frac{mmHg * sec}{ml}$.

2.1.2 Cardiovascular Electrophysiology

With our discussion of cardiovascular mechanics complete, we will now explore the electrophysiological processes that drive the mechanical pumping of the heart. In a healthy heart, electrical impulses originate at the sinoatrial node (SA node), which is a collection of electrically active cells situated in the right atrium abutting the superior vena cava (Figure 2.3). The SA node is the heart's pacemaker, as its electrically active cells normally depolarize spontaneously in a regular fashion. A resultant action potential from such a depolarization propagates through the atria via the myocardium, causing the atria to contract. It subsequently arrives at the atrioventricular node (AV node), which is located at the junction of the atria and ventricles. Action potential conduction through the AV node is slow, which provides sufficient time for the atria to contract and for the ventricles to fill with blood. Subsequently, the action potential passes through the bundle of His and into the Purkinje fibers, which distribute the action potential to ventricles, resulting ultimately in contraction of the ventricles [4].

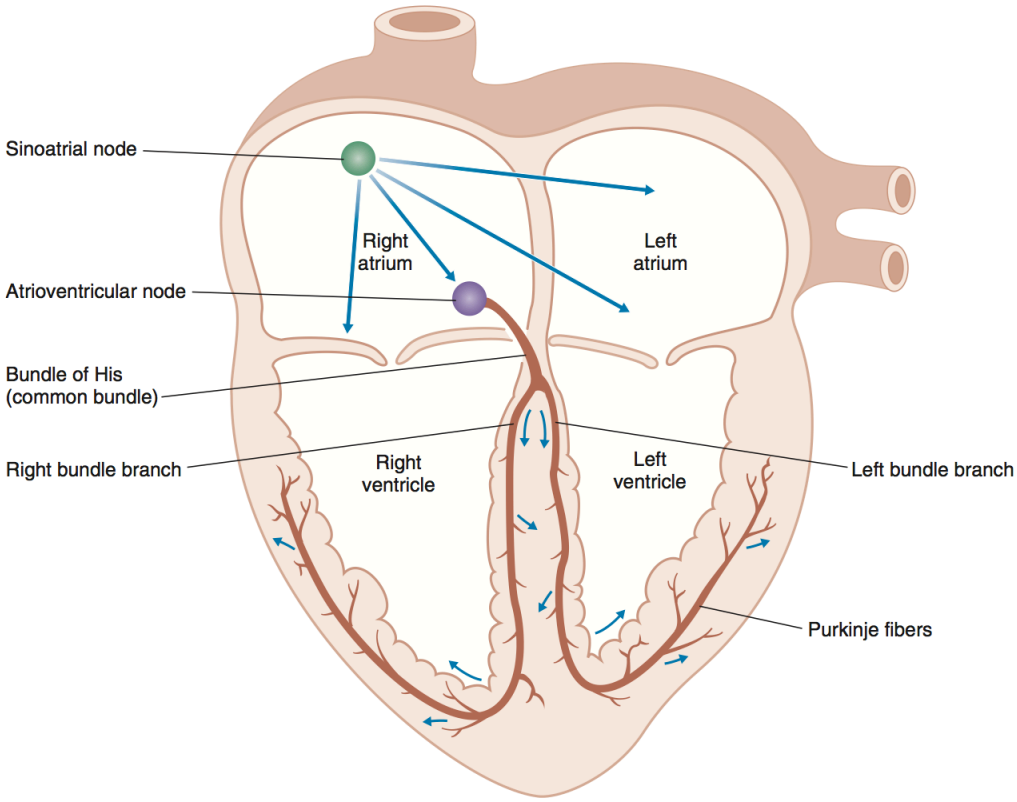

Figure 2.3: Diagram of the heart's electrical conduction system. Taken from [3].

The electrical activity of the heart may be measured using an electrocardiograph (ECG), which records in time the electric potential across various locations on the surface of the body. An ECG trace with the relevant morphological characteristics labeled is provided in Figure 2.4.

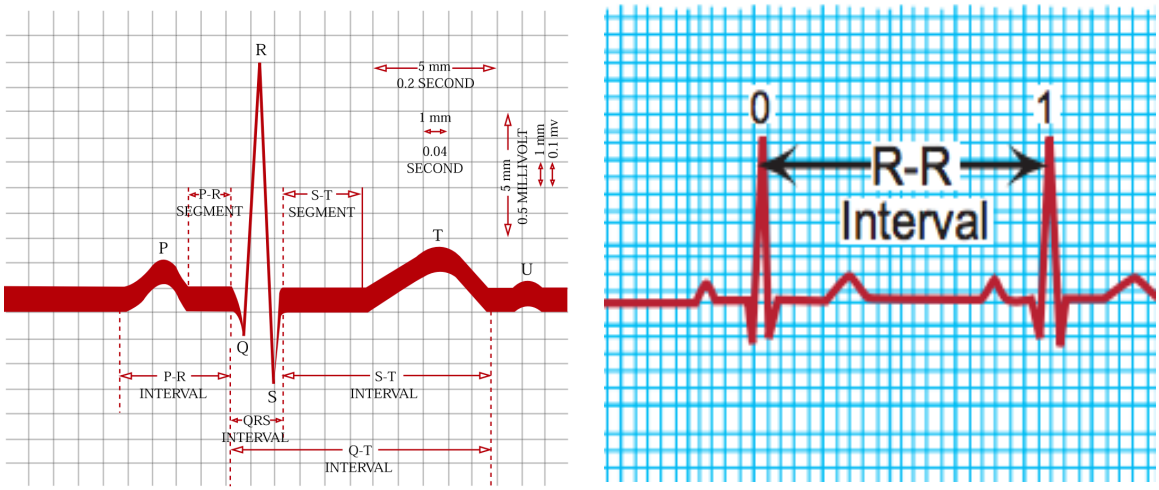

Figure 2.4: Lead II ECG with standard morphological labels (left). The P, QRS complex, and T wave, correspond to atrial depolarization, ventricular depolarization, and ventricular repolarization respectively . Sample measurement of an R-R interval in a lead II ECG trace (right). Both figures taken from [5].

The rhythmic pumping of the heart is divided into beats, *i.e.* one cardiac cycle occurs per beat. One standard measurement for heartbeat duration is the R-R interval (RRI), which we define as the time between two successive R peaks in the ECG. Further, the instantaneous heart rate (HR) at each beat is defined as

$$HR = \frac{60}{RRI} \tag{2.1}$$

with units of beats per minute (bpm). In normal resting humans, HR typically ranges between 60-100 bpm. For the rest of this thesis, RRI will be used as the measurement of heartbeat duration.

2.1.3 Hemodynamics

Equipped with knowledge of the mechanical and electrical foundations of cardiovascular physiology, we will define a few hemodynamic parameters that are central to the understanding of cardiovascular control and our future modeling work in this thesis.

Stroke volume (SV): This is the volume of blood ejected from the heart during a single beat (cycle), measured in milliliters. Mathematically, if V_{ed} is the volume of the left ventricle at the end of isovolumetric contraction, or end of diastole, and V_{es} is the volume at the end of ejection, or end of systole, then we define stroke volume as the difference between these two quantities:

$$SV = V_{ed} - V_{es} \tag{2.2}$$

Cardiac output (CO): This is the volume of blood pumped out of the heart per minute, measured in milliliters/minute. Mathematically, CO is simply the product of heart rate and stroke volume:

$$CO = HR * SV \tag{2.3}$$

Mean arterial pressure (MAP): This is the average arterial pressure during one cardiac cycle and is measured in mmHg. Mathematically, MAP can be expressed as the product of CO and TPR:

$$MAP = CO * TPR = HR * SV * TPR \tag{2.4}$$

2.2 Cardiovascular Control

The cardiovascular system maintains perfusion of oxygenated blood to the central nervous system by controlling blood pressure. The primary mechanism of blood pressure control in the body is the arterial baroreflex, which is mediated by the autonomic nervous system (ANS). We now delve into the details of the ANS and the baroreflex.

2.2.1 Autonomic Nervous System

The autonomic nervous system is a branch of the nervous system that regulates involuntary functions within the body, including blood pressure control, digestion, and arousal. The ANS itself is split into two branches, the sympathetic nervous system (SNS) and the parasympathetic nervous system (PNS), which are colloquially known as the *fight or flight* and *rest and digest* responses, respectively. The PNS is primarily responsible for control of baseline functions such as digestion, urination, and sexual arousal, and it predominates autonomic activity when the body is at rest. In contrast, the SNS is primarily responsible in preparing the body for emergency responses, and it predominates autonomic activity when the body is in a state of stress. In addition to their distinct functions, the two ANS branches also have distinct communication pathways. The PNS acts by releasing the neurotransmitter acetylcholine (ACh) via the vagus nerve, which at the heart then binds to muscarinic ACh receptors, while the SNS acts through the release of epinephrine and norepinephrine via postganglionic nerves [6]. A diagram of these neurochemical pathways is given in Figure 2.5.

Due to their different neurochemical pathways, the effect of the SNS and PNS on the heart can be inhibited roughly independent of each other with the administration of certain pharmacological agents. Drugs that block the binding of ACh to end organ muscarinic receptors will shut off the PNS's cardiac effector mechanism without impacting the SNS's cardiac effector mechanisms. Likewise, drugs the block the binding of epinephrine and norepinephrine to end organ beta receptors will shut off the SNS's main cardiac effector mechanism without impacting the PNS's cardiac effector mechanism. Two pharmacological agents that will be used later in this thesis are

propranolol and atropine. Propranolol is a competitive antagonist with epinephrine and norepinephrine at beta receptors, blunting the SNS's cardiac effector mechanisms. Atropine is a muscarinic competitive antagonist that effectively blocks ACh binding with muscarinic receptors at the heart [3].

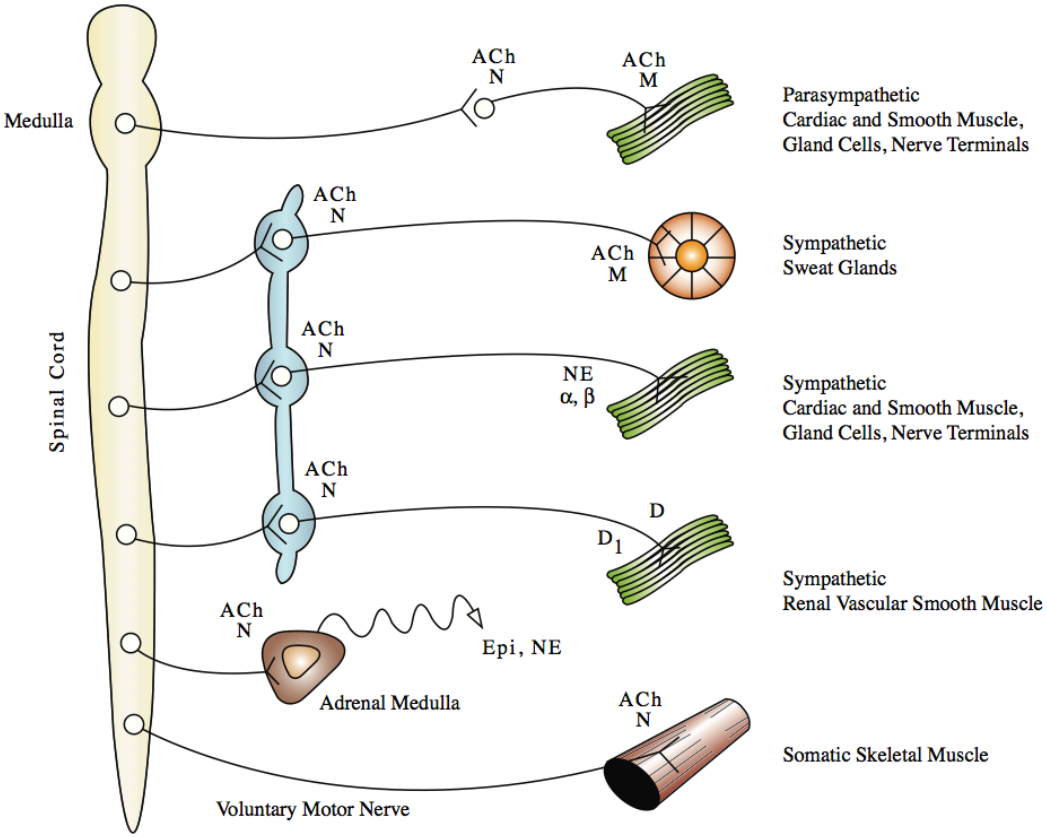

Figure 2.5: Sketch of the ANS's neurochemical pathways. ACh, NE, Epi, and D, represent the acetylcholine, norepinephrine, epinephrine, and dopamine neurotransmitters, respectively. M, N, α, and β, represent the muscarinic, nicotinic, alpha, and beta receptors respectively. Taken from [6].

2.2.2 Arterial Baroreflex

The arterial baroreceptors are stretch receptors that line the walls of the carotid artery as well as the aortic arch (Figure 2.6). As the arterial walls stretch in response to changes in blood pressure, the baroreceptors transmit electrical impulses via the carotid sinus and aortic nerves to the brain. The impulse firing rate increases as the transmural pressure at

the baroreceptors increases. These impulses are then relayed to the brain, where the medulla integrates them and decides how to adjust blood pressure, subsequently assigning actions to the PNS and SNS. From Equation 2.4, it is clear there are three factors that can modulate blood pressure; heart rate, stroke volume, and total peripheral resistance. The ANS has the ability to alter all three.

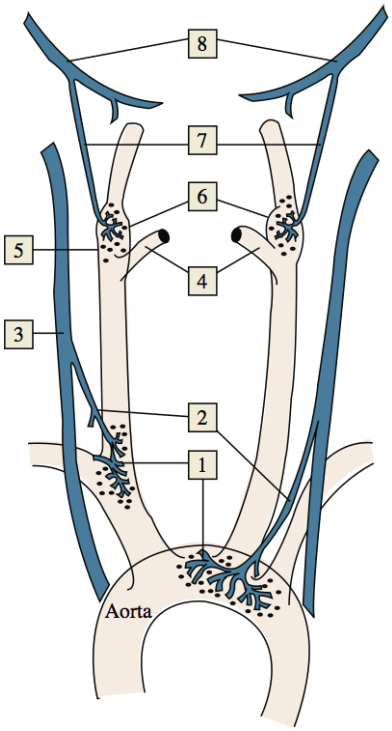

1. *Aortic baroreceptors*
2. *aortic nerves (depressor branches of vagi)*
3. *vagus nerve*
4. *external carotid artery*
5. *carotid sinus*
6. *carotid baroreceptors*
7. *carotid sinus nerves*
8. *glossopharyngeal nerves*

Figure 2.6: Sketch of the baroreceptors and their efferent pathways to the brain. Taken from [6].

The SA node is innervated by both sympathetic and parasympathetic fibers, enabling heart rate control by both the PNS and SNS. Parasympathetic control of heart rate is fast, occurring on the timescale of 0.5-2 seconds, whereas sympathetic control of heart rate is relatively slow, occurring on the timescale of 2-10 seconds. Recognizing the varying timescales and delays of the sympathetic and parasympathetic heart rate effector mechanisms will prove useful in the next chapter, where we model the baroreflex and attempt to disambiguate the two branches of the ANS.

While heart rate may be significantly regulated by both branches of the ANS, cardiac contractility and vascular resistance are primarily regulated by the SNS, as both cardiac and vascular smooth muscle are largely innervated by the SNS. The SNS can increase the tension in the vascular smooth muscle, which causes an increase in peripheral resistance. Similarly, the SNS can increase the tension in cardiac smooth muscle, raising cardiac contractility and consequently the stroke volume [7].

Thus far we have introduced the baroreflex as a short-term blood pressure control mechanism that works to maintain the pressure at some set-point. In the long-term, however, this set-point is not constant. Specifically, the blood pressure set-point is subject to change depending on varying conditions such as posture, level of physical exertion, or hypertension. Moreover, the predominance of one branch of the ANS over the other also depends on a person's state, as discussed in Section 2.2.1. With respect to posture, it has been shown that when moving from a supine to tilted/upright posture, the balance between the PNS and SNS in the body swings from greater PNS control to greater SNS control [8]. In later parts of this thesis, varying postures will be one set of experimental conditions.

2.3 Heart Rate Variability

Heart rate variability (HRV) is the natural variation in beat-to-beat heart rate caused by factors such as thermoregulation, baroreflex, and circadian rhythms. A great amount of literature is devoted to examining HRV, and using it to develop a deeper understand of autonomic control of the cardiovascular system. While HRV has been examined in both the time and frequency domains, the frequency domain analyses are most salient to this thesis.

Frequency domain HRV analysis focuses on extracting the power spectrum of the heart rate signal from subjects under various experimental conditions [9]. Prior work elucidated the frequencies at which the ANS controls heart rate by selective blockade of the SNS and PNS and examination of the resulting power spectra. Specifically, heart rate fluctuations in the frequency range of 0.04-0.5Hz have been found to correspond to autonomic control of heart rate in adults [10]. Within this 0.46Hz band, two sub-bands have been roughly demarcated, the low frequency band (LF) ranging from 0.05-0.15Hz and the high frequency band (HF) ranging from 0.15-0.4Hz [11].

Power in the HF band is driven primarily by the PNS and respiration, while power in the LF band is driven by both the PNS and SNS. Within the LF band there is typically a significant peak between 0.10-0.15Hz, which corresponds to fluctuations known as the Mayer waves. Prior studies have shown that opening the baroreflex control loop results in a loss of the Mayer waves, suggesting that Mayer waves are formed by a resonance in the control system [12]. While there is generally very little power in the frequencies above the HF band, there is significant power in the frequencies lower than the LF band, *i.e.* 0.0-0.04Hz. The underlying physiological mechanism for these sub-LF fluctuations is still unknown, but it was hypothesized that they are due to thermoregulation and circadian rhythms [13].

One metric for autonomic balance that emerged from HRV analysis is the LF/HF index, defined as the quotient of the total power in the LF band by the total power in the HF band [14]. Although LF/HF gained substantial popular in physiological literature, its underlying assumption that LF power is primarily due to sympathetic control of heart rate is in stark contrast to the observation that both

the PNS and SNS make significant contributions to LF. As LF is not unambiguously a measure of sympathetic activity, LF/HF is an inherently poor metric [15]. Our work in this thesis attempts to address some of the shortcomings of HRV analysis, such as the ambiguity in autonomic contributions to the LF region.

Chapter 3

Open-Loop Modeling of Baroreflex and Baroreflex Sensitivity

While the ultimate goal of this chapter is to determine how to quantify the action of the baroreflex, we must first define both a model and a metric for baroreflex activity. The discussion of heart rate variability in the preceding chapter leads to a natural starting point for this task. That is, observed fluctuations in heart rate may potentially be explained by fluctuations in blood pressure via baroreflex control. In this chapter, we formulate both a black-box and a parametric open-loop model to describe the behavior of the heart-rate arc of the baroreflex, and subsequently develop measures of baroreflex activity for each model.

3.1 Open-loop response and Baroreflex Sensitivity

Open-loop baroreflex function is well described, dating back to the rabbit experiments performed by Eberhard Koch in 1931 [16]. In particular, Koch's experiments demonstrated that open-loop control of blood pressure results in a sigmoidal response in

R-R interval (RRI). Koch cleverly opened the baroreflex loop by clamping the common carotid arteries beneath their respective carotid sinuses, and independently varying the pressure applied to the baroreceptors [17]. While Figure 3.1 shows a sketch of a single SBP→RRI response curve, the baroreflex constitutes an ensemble of sigmoidal responses. Each response in the ensemble is a realization of the baroreflex under a certain set of physiological conditions. Different physiological stresses result in both distinct operating points (centers) and distinct slopes for the sigmoidal characteristic [18]. In addition, physiological variability between individuals results in a different ensemble of baroreflex curves for each individual.

For each response curve, we define baroreflex sensitivity (BRS) as the slope of the curve at the operating point, i.e. the slope in the linear region of the sigmoid [18]. In the next chapter, we will use BRS as one metric of baroreflex activity.

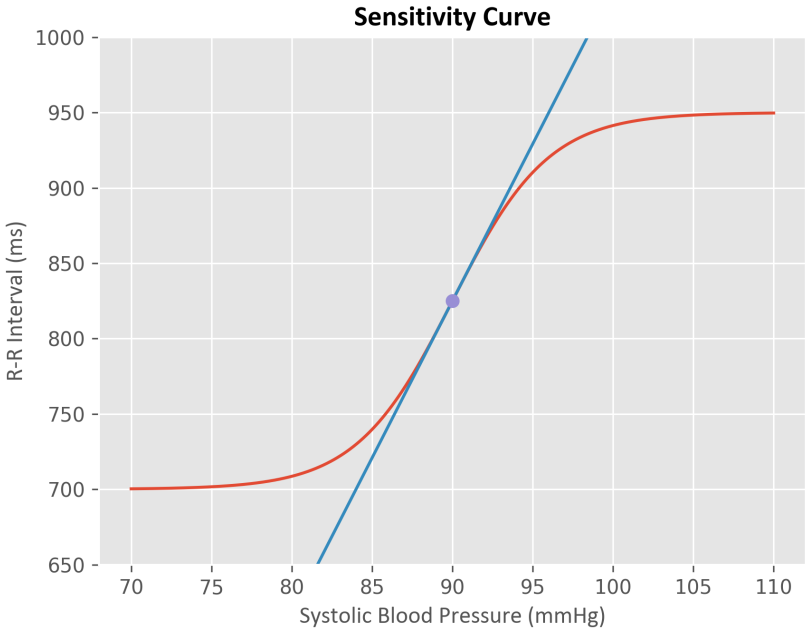

FIGURE 3.1: Illustrative cartoon of the sigmoidal response in RRI to incremental changes in systolic blood pressure (SBP). The purple dot indicates the operating point of this specific baroreflex curve, which is set to a SBP of 90 mmHg and an RRI of 825 ms. The blue line is the tangent line of the sigmoid at the operating point. Note that as distance from the operating point increases, the slope of the sigmoid decreases.

3.2 Black-box Open-loop Model

Using a model will let us build intuition for the system and will be useful for relating our observations to BRS. We thus present the assumptions of our model:

Open-loop: Though the human baroreflex is a closed-loop control system, we shall temporarily consider a simpler model assumption where it is open-loop. In addition, this open-loop model will not make any assumptions about the system parameters, but rather, it will consider the system relating SBP to RRI as a black-box.

Time invariance: Given relatively short time durations and steady-state conditions[1], the response of the baroreflex is time invariant, i.e. the baroreflex is operating along a single response characteristic [19]. In practice, this assumption becomes a condition on data used for analysis, specifically limiting our model to stationary (in the wide sense) signals [20].

Linearity: Our assumption of time invariance coupled with the observation that most spontaneous RRI/SBP fluctuations occur near the operating point (linear region) of the baroreflex allows us to make the assumption that the response of RRI to changes in SBP is linear [21]. Consequently, we fix the origin of our model as the set-point of the response.

[1] We define steady-state conditions as the state where the stresses on the body are constant and all transients have died down. Examples of steady-state conditions are lying down in a fixed position or jogging at a constant rate on a controlled surface such as a treadmill. Examples of transients would be the movement from standing to sitting, or walking to jogging.

Our overall model for the baroreflex is thus an open-loop LTI controller with systolic blood pressure as the input and RRI as the output, as shown in Figure 3.2. It is important to note that our model only attempts to explicitly characterize the behavior of the heart rate control arc of the baroreflex. As mentioned in the prior chapter, the baroreflex controls not only heart rate, but cardiac contractility and peripheral vascular tone as well. Implicitly, BRS may contain information regarding the activity of non-heart-rate arcs. A decline in BRS, for example, could indicate a shift from control of heart rate to control of peripheral vascular tone while total heart rate arc baroreflex activity remains constant.

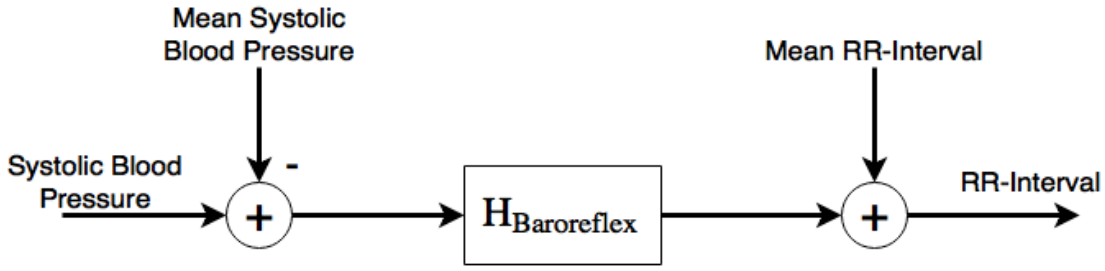

Figure 3.2: Open-loop, black-box model for baroreflex.

3.3 Measuring Baroreflex Sensitivity

Now that we have defined BRS as our metric for baroreflex activity, we need to estimate it. BRS can be computed in both the time domain and the frequency domain. Time domain techniques for estimating BRS are based on the sequence method pioneered by Di Rienzo *et al.* [22]. The sequence method obtains sequences of consecutive heartbeats where SBP and RRI are simultaneously monotonically increasing or simultaneously monotonically decreasing (typically sequences of three or more beats), finds the RRI-SBP slope for each sequence, and takes the mean of the slopes over all selected sequences. This computed mean of slopes is Di Rienzo's time domain BRS estimate. The sequence method, however, suffers from several deficiencies. First, by only considering

sequences of consecutive beats, the method acts as an implicit high-pass filter that neglects the sympathetic contribution to baroreflex due to the relatively long timescale of sympathetic activity [23]. Second, since the sequence method may sample sequences of RRI and SBP that lie far from the operating point, the slopes computed from these sequences may be much smaller than the slope at the operating point, which leads to underestimates of BRS. A common adjustment to the second problem is the requirement that the slope of any sequence included in the final slope average must be above a minimum threshold [24]. Nevertheless, because this adjustment requires an *a priori* judgment of the shape of the baroreflex characteristic for a given subject and setting, it is not a robust estimator, and also cannot be used in real time.

Most frequency domain methods for estimating BRS are based on the transfer function method defined by deBoer *et al.* (1985) [25]. The transfer function method computes the spectral transfer function from the SBP time series to RRI time series, and estimates BRS as the magnitude of that transfer function in the low frequency (0.04-0.15Hz) band. Mathematically, this transfer function is represented as $H\left(f\right) = \frac{S_{BR}}{S_{BB}}$, where S_{BR} is the cross-spectrum between the SBP time series and the RRI time series, and S_{BB} is the auto-spectrum of the SBP time series. Since the transfer method focuses on low frequency fluctuations, it does not implicitly filter out sympathetic contributions (unlike the sequence method), but explicitly filters much of the fluctuation due to respiratory activity, ultimately improving accuracy [26]. Additionally, this method provides phase information, which can be helpful in elucidating relationships such as causality or potentially autonomic balance. While the sequence method and its variants are simpler to implement than the transfer function method, this shortcoming is

outweighed by the advantages in estimation accuracy and phase information provided by the transfer function method. We accordingly use the transfer method in all following analyses of the black-box model in this document. Our specific implementation of the transfer function method is described in detail in Appendix A.

3.4 Parametric Open-loop Model

We will now develop a parametric model follows the same assumptions from the model in Section 3.2 but varies in structure. First, we directly model both the sympathetic and parasympathetic components of the baroreflex response, $H_{Baroreflex}$. Second, the time evolution of this model is beat-to-beat, i.e. the time unit of our discrete time model is one beat. Third, we adjust our output variable from R-R interval to heart rate (HR). Our parametric model for the baroreflex is thus an open-loop LTI controller with systolic blood pressure as the input and HR as the output, evolving in time on a per beat basis.

The foundation for the parametric system model comes from the work of Chen and Mukkamala as shown in Figure 3.3 [27], who synthesized the description of the sympathetic and parasympathetic impulse responses in dogs by Berger *et al.* [28] and the system identification work of Mullen *et al*. [29]. By visual inspection, we model the parasympathetic impulse response as a gain, and the sympathetic impulse response as a damped, second-order system. The total baroreflex response is therefore the sum of the two individual responses since the individual responses are assumed linear. Mathematically this is given by Equation 3.1, and is shown schematically in Figure 3.4:

$$H_{Baroreflex}(z) = H_p(z) + H_s(z) = K_p + \frac{K_s z^{-1}}{(1-\beta z^{-1})^2} \tag{3.1}$$

Though we will primarily focus on the model above in this thesis, we will also explore variations where the parasympathetic impulse response is either a two tap, or three tap finite impulse response of the form:

$$H_{p2}(z) = K_p + K_{p1}z^{-1} \tag{3.2A}$$

$$H_{p3}(z) = K_p + K_{p1}z^{-1} + K_{p2}z^{-2} \tag{3.2B}$$

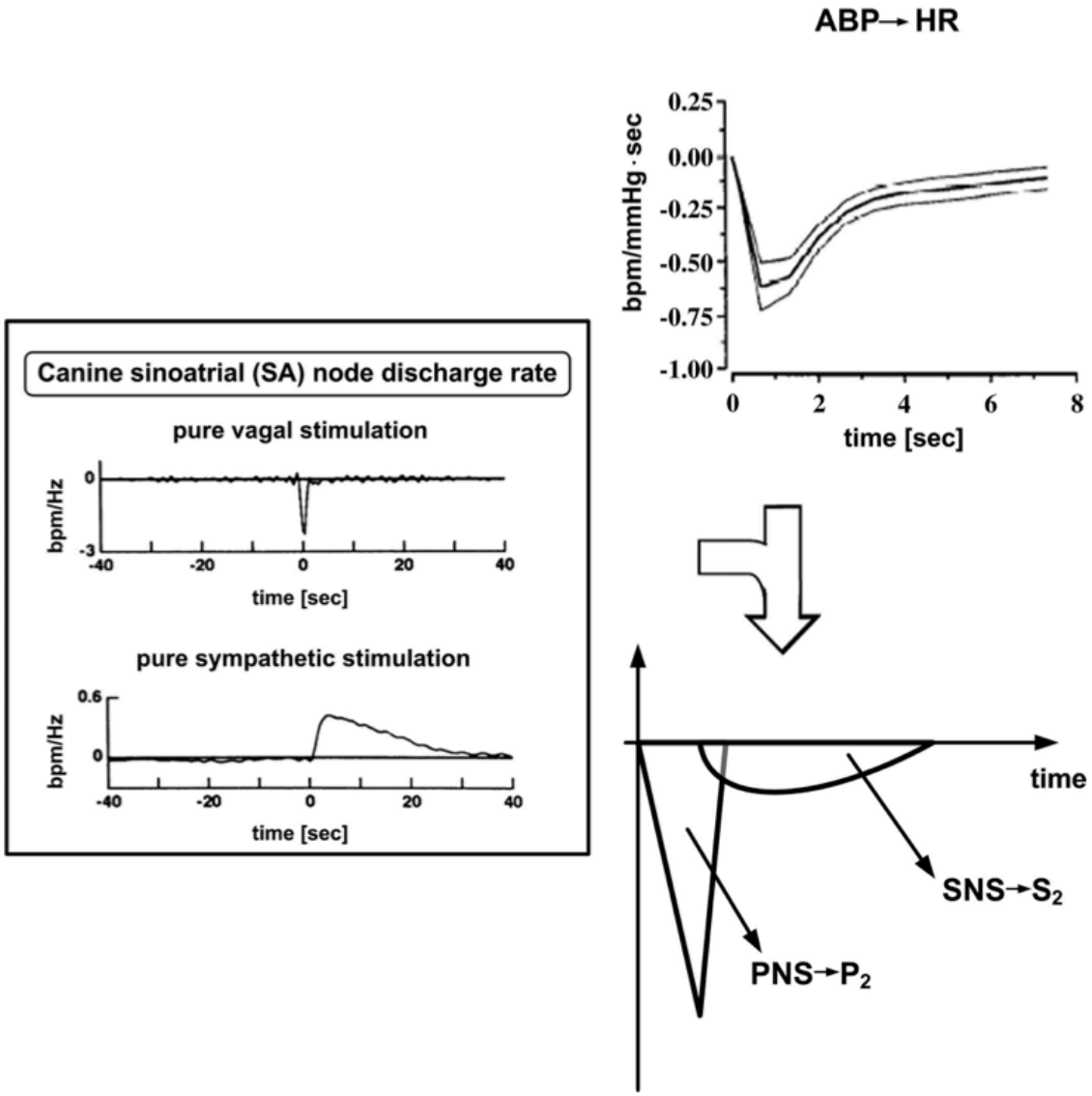

Figure 3.3: Left: The canine's parasympathetic impulse response (top), and sympathetic impulse response (bottom) [28]. Top Right: ABP→HR transfer function in humans [29]. Bottom Right: Decoupling of parasympathetic and sympathetic effects on the ABP→HR transfer function [27]. Full figure taken from [27].

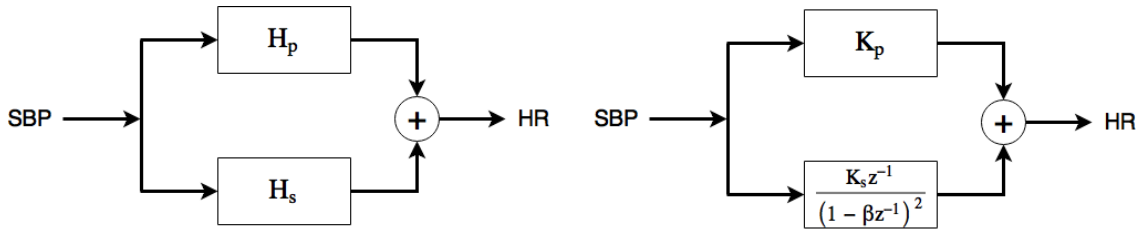

Figure 3.4: Overall open-loop parametric model for baroreflex. The diagram on the left displays the two sub-systems, one for each branch of the autonomic nervous system. The diagram on the right displays the parameterizations of the two branches.

For any given baroreflex response, we can define the parasympathetic-sympathetic ratio (PSR) as $\frac{A_p}{A_p+A_s}$ where A_p and A_s are the actions of the parasympathetic and sympathetic impulse responses, respectively [30]. We define the signal action $A_i = \sum_{k=-\infty}^{\infty} |h_i[k]|$, where h_i is the system impulse response, which for the system given by Equation 3.1, yields the following PSR:

$$PSR = \frac{K_p}{K_p + \frac{K_s}{(1-\beta)^2}} \tag{3.3}$$

This metric is an assessment of autonomic balance and will be used throughout the thesis to validate the parametric model and compare varying states of the baroreflex. Finally, with a beat-to-beat model, frequency domain analyses become more complicated because the model assumes that heartbeats are uniform in duration, i.e. each time step is the same [31]. As a consequence, the parametric model is not amenable to the same transfer function method that the black-box model is. With the parametric model, we therefore will use the PSR, as well as the parasympathetic and sympathetic gains, K_p and K_s, in order to determine autonomic balance and baroreflex activity. In the next chapter we will proceed to analyze the black-box and parameterized open-loop models.

Chapter 4

Open-loop Model Analysis

With a metric (baroreflex sensitivity) and measurement method (transfer function analysis) for baroreflex activity defined in Chapter 3, we will now apply the method and establish what information it provides. While there is no standard measurement for baroreflex activity, the metric can be analyzed using data from a dual pharmacological blockade and postural study. Specifically, the physiological interventions in these studies affect autonomic balance in predictable ways, as outlined in Chapter 2, allowing us to calibrate our understanding of the method. In addition, we perform parameter estimation on our parametric open-loop model from Section 3.4, and determine its ability to model the baroreflex.

4.1 Experimental Data Set

For validation we used data from a simultaneous pharmacological blockade and postural study performed by Saul *et al.* [32]. Arterial blood pressure (arterial line measurement) and ECG recordings (sampled at 360Hz) were collected from fourteen nonsmoking adult

males, without any history of cardiopulmonary disease. Initially, data were recorded for each subject in the supine position for thirteen minutes, and then in the standing position for thirteen additional minutes. Afterwards, all subjects were returned to the supine state. Half of the subjects were administered atropine, a parasympathetic blocking agent, while the other half were administered propranolol, a sympathetic blocking agent. Data were again collected using the same postural protocol as before. Subsequently, all subjects were returned to the supine position and were administered the other autonomic blockade drug (atropine if they received propranolol first, and propranolol if they received atropine first). Data were then collected again for a final time using the initial postural protocol. Sufficient time was given between moving from supine to standing, as well as after the administration of autonomic blockade agents to allow for physiological equilibration. The experimental protocol is explained in greater depth in Saul *et al.* [32, 33].

Let us now define the term *subject-state*, as the data collected from an experimental subject while the subject was under a certain experimental condition. An example of a subject-state would be the data collected for Subject 11 while in the supine position after the administration of propranolol. For notational simplicity, each subject-state is represented by a unique five-character identifier, which will be used throughout this thesis. The first two characters are the subject identifier, ranging from '01' to '14'. The next two characters are the postural states with either the letters 'ST' for standing or 'SU' for supine. The final character represents the prevailing pharmacological state, with 'C' indicating **c**ontrol (no blockade), 'P' indicating **p**ropranolol first, 'A' indicating **a**tropine first, and 'B' indicating the application of **b**oth blockers. With 14 subjects and 6 states per subject (2 tilting positions multiplied by 3 pharmacological conditions), we

theoretically have a total of 84 subject-states. Our dataset, however, only contains recordings from 79 subject-states, as 5 of the 84 combinations were not available.

4.2 Transfer Function Analysis

For each subject-state, we extracted the RR-interval (RRI) time series from the ECG recording and the systolic blood pressure (SBP) time series from the arterial blood pressure recording. We then computed the RRI and SBP power spectra, the transfer function from SBP to RRI, and the baroreflex sensitivity (BRS) as detailed in Chapter 3. Further details of our transfer function and BRS computations are available in Appendix A, in addition to the full set of computed BRS values.

4.2.1 Results

In the control state, all subjects exhibited a decrease in BRS between the supine position and the standing position, with a mean decrease of 12.7 ± 6.3 ms/mmHg, which is summarized in Figure 4.1. Physiologically, human vagal tone tends to be stronger in the supine position and weaker in the standing position, while sympathetic tone tends to be stronger in the standing position and weaker in the supine position. Hence, the categorical decrease in BRS as a result of moving from the supine to the standing state suggests that BRS is strongly sensitive to parasympathetic activity, as it tracks the expected change in vagal tone.

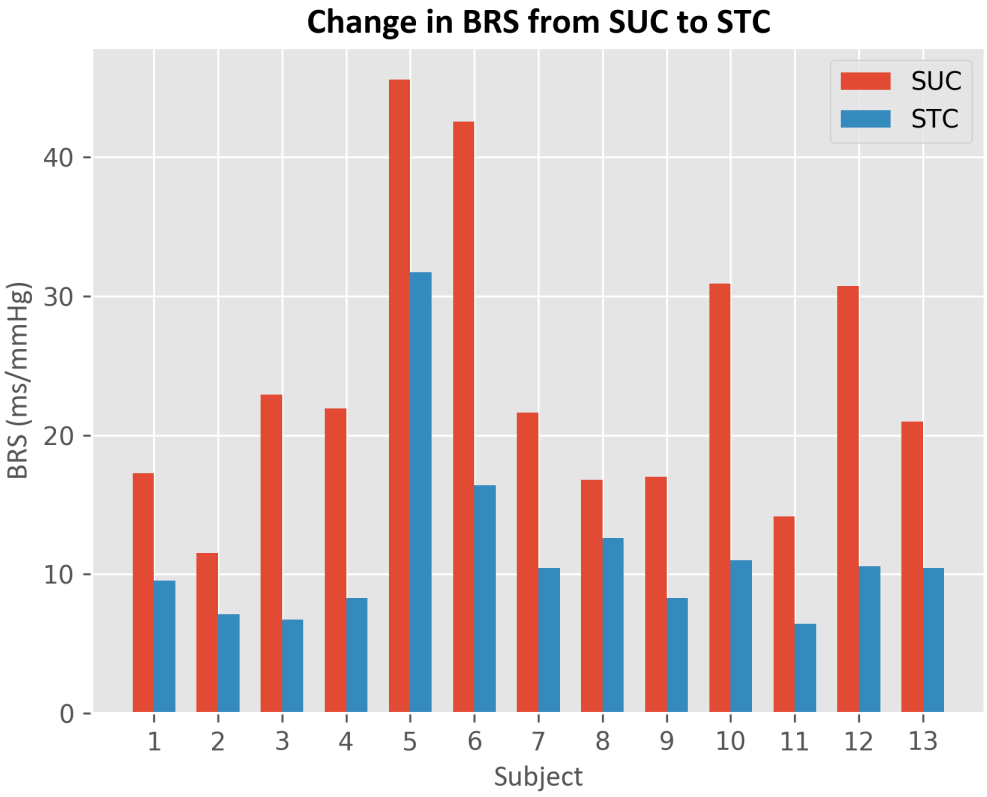

FIGURE 4.1: BRS values from supine (SUC) to standing (STC) without pharmacological intervention.

With respect to pharmacological interventions, the application of atropine resulted in a significant drop in BRS for each subject (mean decrease of 17.6 ± 11.0 ms/mmHg) as displayed in Figure 4.2, which shows the BRS values before and after the application of atropine, both times in the supine state, in subjects in whom atropine was administered first. We compare BRS values in the supine position to isolate the effect of atropine on vagal regulation of heart rate, since changing posture from the standing to supine state shifts autonomic balance by increasing parasympathetic activity and reducing sympathetic activity. The overall effect of blocking parasympathetic activity is a significant reduction in BRS, as was the case in moving from supine to standing (Figure 4.1).

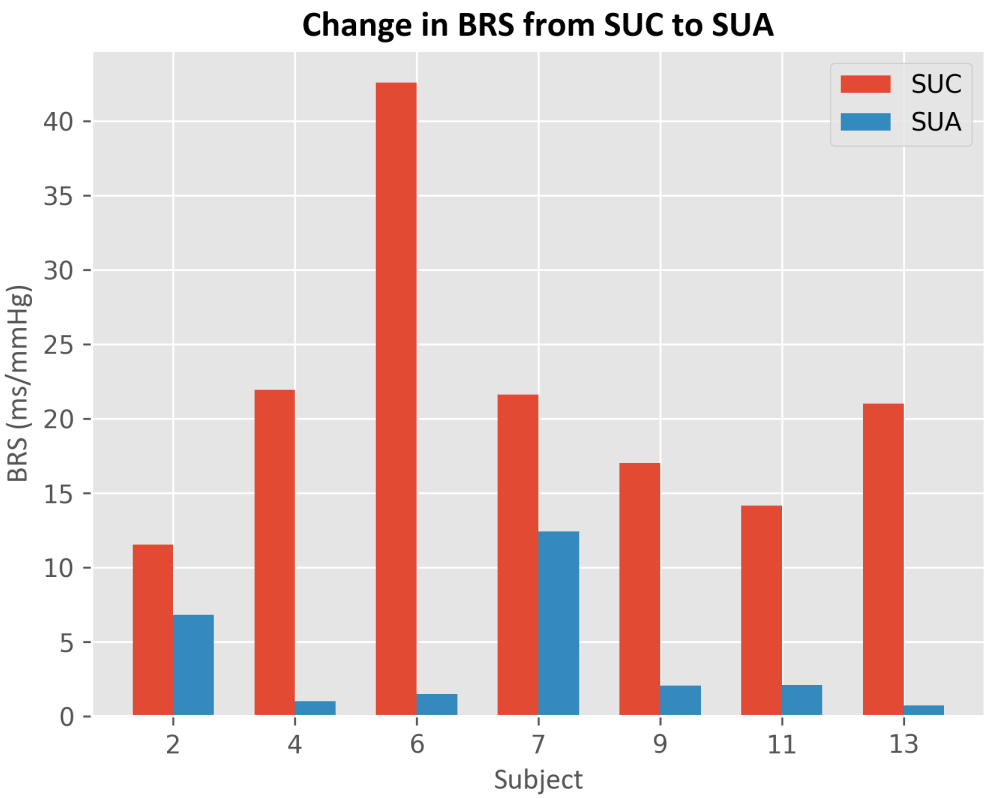

FIGURE 4.2: BRS values from supine and no pharmacological blockade (SUC), and supine after application of atropine (SUA).

Meanwhile, the application of propranolol resulted in a slight increase in BRS for most of the subjects (mean increase of 2.1 ± 2.6 ms/mmHg) as displayed in Figure 4.3 which shows the BRS values before and after the application of propranolol, both times in the standing position for subjects who were given propranolol first. In contrast to the atropine intervention, we report BRS values in the standing position to isolate the effect of propranolol on sympathetic regulation of heart rate.

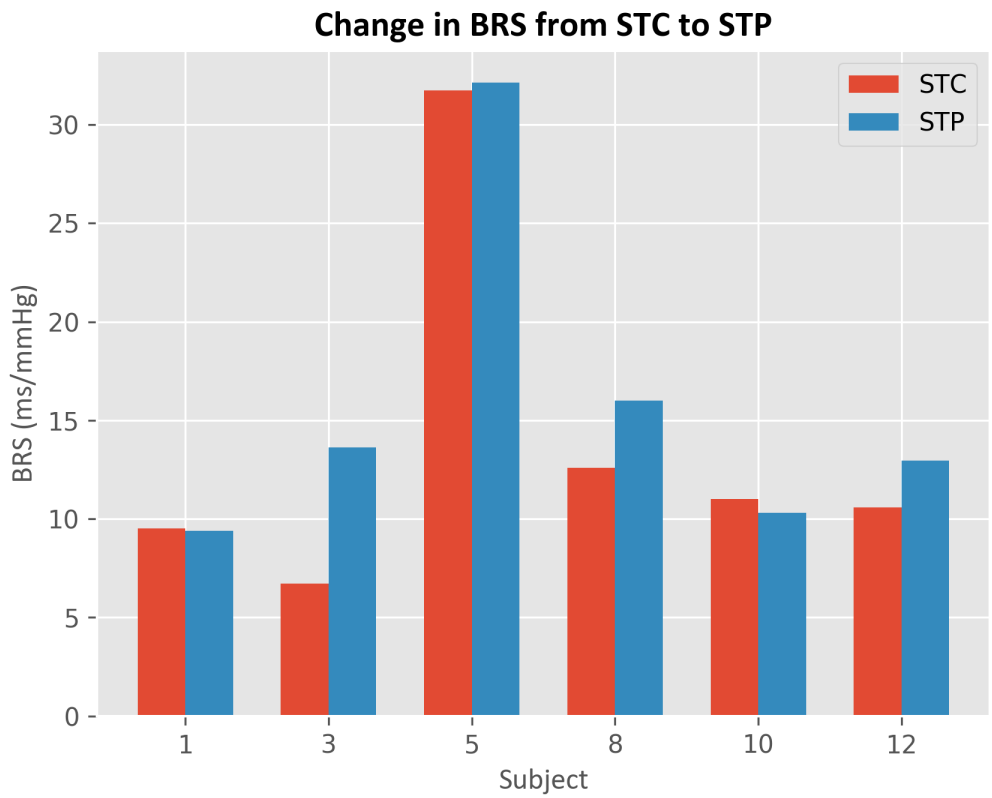

FIGURE 4.3: BRS values from standing and no pharmacological blockade state (STC), and standing with application of propranolol (STP).

The effect of pharmacological blockade on BRS is clearly substantial, as illustrated by Figures 4.2-4.3. The drop in BRS with the application of atropine, the parasympathetic blocker, and very slight rise in BRS with the application of propranolol, the sympathetic blocker, are consistent with the hypothesis that BRS (as determined by the transfer function method) is a sensitive measure of parasympathetic activity. Physiologically, the slight rise in BRS after the application of propranolol may indicate that in the absence of one branch of autonomic control, in this case the sympathetic branch, the other branch is utilized at a greater rate.

Other analyses on this dataset have yielded similar results, though by exploring separate metrics of autonomic activity and balance. Xiao investigated the connection between respiratory rate and autonomic balance, and identified a metric for

parasympathetic activity, the *parasympathetic index*, as the peak of the impulse response relating instantaneous lung volume to heart rate [34]. Xiao's parasympathetic index decreased as the subjects shifted from the supine to standing postures, and after the application of atropine. These changes to parasympathetic index are in concordance with the changes we observed in BRS.

4.3 Open-loop Parameter Estimation

We will now formalize the parameter estimation problem for the model defined in Section 3.4. Recall that in the one-tap model our system transforms SBP to HR governed by a Z-transform of the form

$$H_{Baroreflex}(z) = K_p + \frac{K_s z^{-1}}{(1-\beta z^{-1})^2} \tag{4.1}$$

If we simulate the dynamics of the system with a given input SBP time series, $\overrightarrow{SBP}$, then the output of the system will yield an estimated HR time series, $\overrightarrow{\widehat{HR}}$, dependent upon the given collection of system parameters $\vec{\theta} = [K_p \quad K_s \quad \beta]$. We will define our optimization criterion as the ℓ_2 norm of the vector difference between the true HR time series, $\overrightarrow{HR}$, and $\overrightarrow{\widehat{HR}}$.

$$\mathcal{C} = \left\| \overrightarrow{HR} - \overrightarrow{\widehat{HR}} \right\|_2 \tag{4.2}$$

If we let $\overrightarrow{\widehat{HR}}$ be a function of $\vec{\theta}$, then we can frame our estimation problem as determining some $\vec{\theta}_{min}$ that minimizes $\mathcal{C}$:

$$\vec{\theta}_{min} = \underset{\vec{\theta}}{\operatorname{argmin}}\, \mathcal{C} = \underset{\vec{\theta}}{\operatorname{argmin}} \left\| \overrightarrow{HR} - \widehat{\overrightarrow{HR}(\vec{\theta})} \right\|_2 \tag{4.3}$$

Finally we consider what length of data enables robust parameter estimation. In Section 3.2 we made the assumption that given a sufficiently small window of time our system is time invariant and the signal statistics are stationary. The longer the stretch of data, however, the weaker this assumption becomes. Hence, estimating parameters over too large a window of data may result in poor model fit. In contrast, estimating parameters over a window of data with too few beats may result in overfitting to noise, significant window-to-window variation in parameter estimates, and poor generalizability. For the remainder of this thesis, we will use a window length of 60 beats, which empirically serves as a compromise between signal stability and proper conditioning of the parameter estimation problem. Furthermore, a 60 beat window is considerably longer than the timescale of the slowest cardiovascular control systems of interest, which ranges from 8-12 beats. If we take an input data series of length *N*, and segment it into non-overlapping data windows of length *M*, then we have $W = \left\lfloor \frac{N}{M} \right\rfloor$ windows, where $\lfloor\ \rfloor$ represents the floor function. Performing windowed estimation ultimately yields an ensemble of W values for each model parameter per subject-state recording, which we designate as the *parameter ensemble*.

With the estimation problem given in Equation 4.3, we performed windowed parameter estimation for the one-tap, two-tap, and three-tap open-loop models on each of the seventy-nine subject-state recordings. Minimization was achieved using the Basin-Hopping algorithm (unconstrained), a stochastic global optimization method [35]. Specifically, Basin-Hopping combines Monte Carlo sampling with local minimization

performed at each step [36]. For each subject-state the true demeaned heart rate and estimated demeaned heart rate time series were obtained. Additionally, parameter ensembles for each subject-state were saved, and the mean and variance of each parameter ensemble were computed. Figure 4.4 shows an example of the true and estimated demeaned heart rates together, as well as the corresponding parameter ensembles used to generate the optimal estimated heart rate for subject-state given the one-tap model.

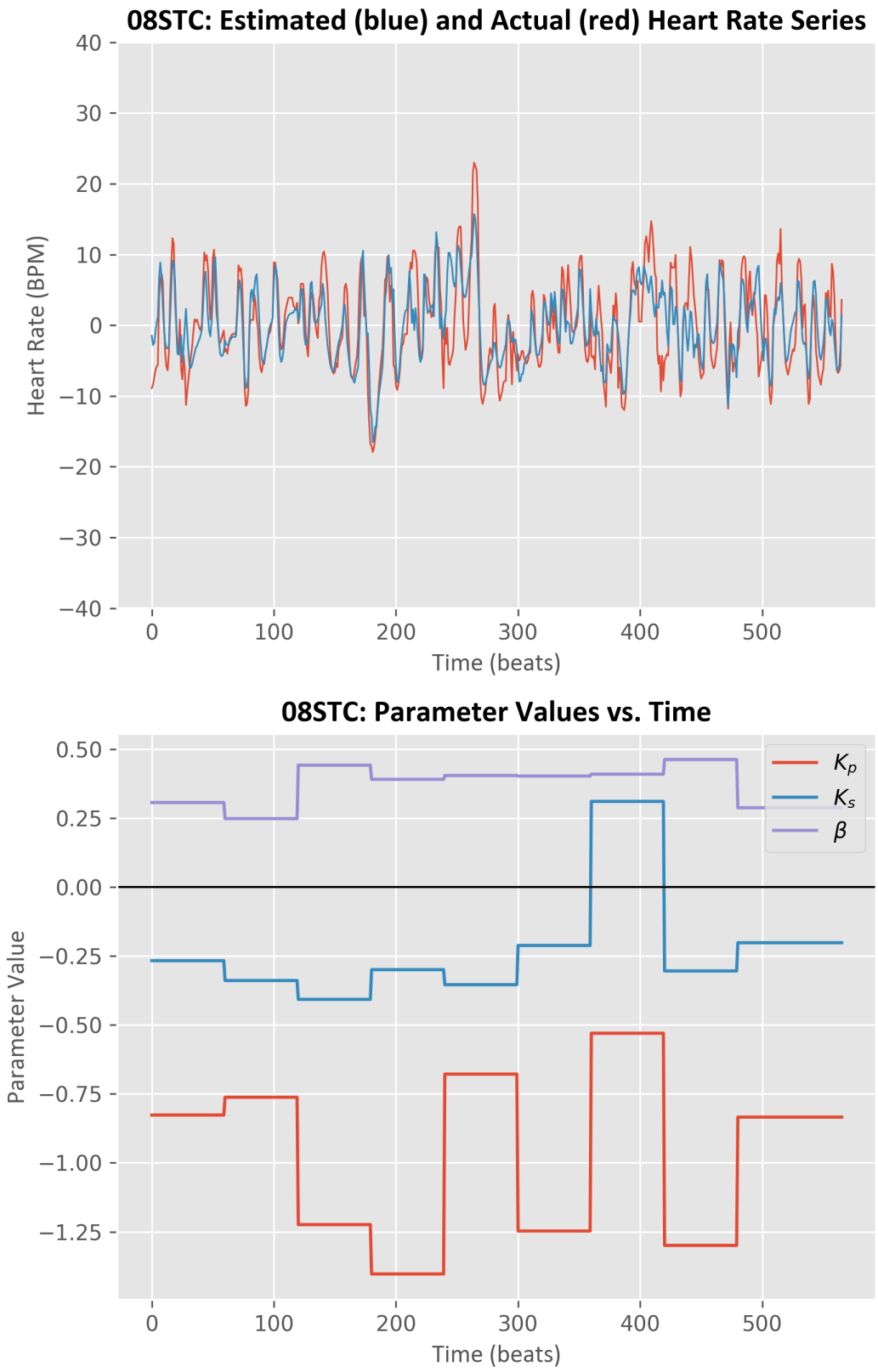

FIGURE 4.4: SBP time series comparison plot for 08STC (top) and the estimated model parameters over time (bottom). The RMSE between the true and estimated heart rate time series for this recording is 4.0 bpm. The units of K_p, K_s, and β are $\frac{bpm}{mmHg}$, $\frac{bpm}{(beat)*(mmHg)}$, and $\frac{1}{beat}$ respectively.

In each ensemble, parameter estimates from windows that did not cohere well to the model assumptions were excluded in the parameter mean and variance computations. We describe a window as having good coherence to the model assumptions if the true HR and SBP signals move in opposite directions, i.e. that the two signals are roughly 180° out of phase. Prior to the parameter estimation, this is a very difficult task to automate given the nature of the signals. It was observed, however, that the estimated heart rate signal from windows with poor model coherence often exhibited significantly less variation than the true heart rate signal. This was not the case for estimated heart rate signals from windows that cohered well with the model. Signal variance was therefore determined to be a good heuristic for model coherence, and the criterion for window inclusion in the parameter ensembles was:

$$Var\left(\overrightarrow{\widehat{HR}}\right) > 0.2 * Var(\overrightarrow{HR}) \tag{4.4}$$

For the one-tap model, 135 out of a total 787 windows (over the 83 recordings) were excluded, and in terms of subject-states, 57 out of the 83 subject-state recordings had windows excluded. An example of a subject-state that coheres well with the model is shown in Figure 4.5, while an example of a subject-state that coheres poorly with the model is shown in Figure 4.6.

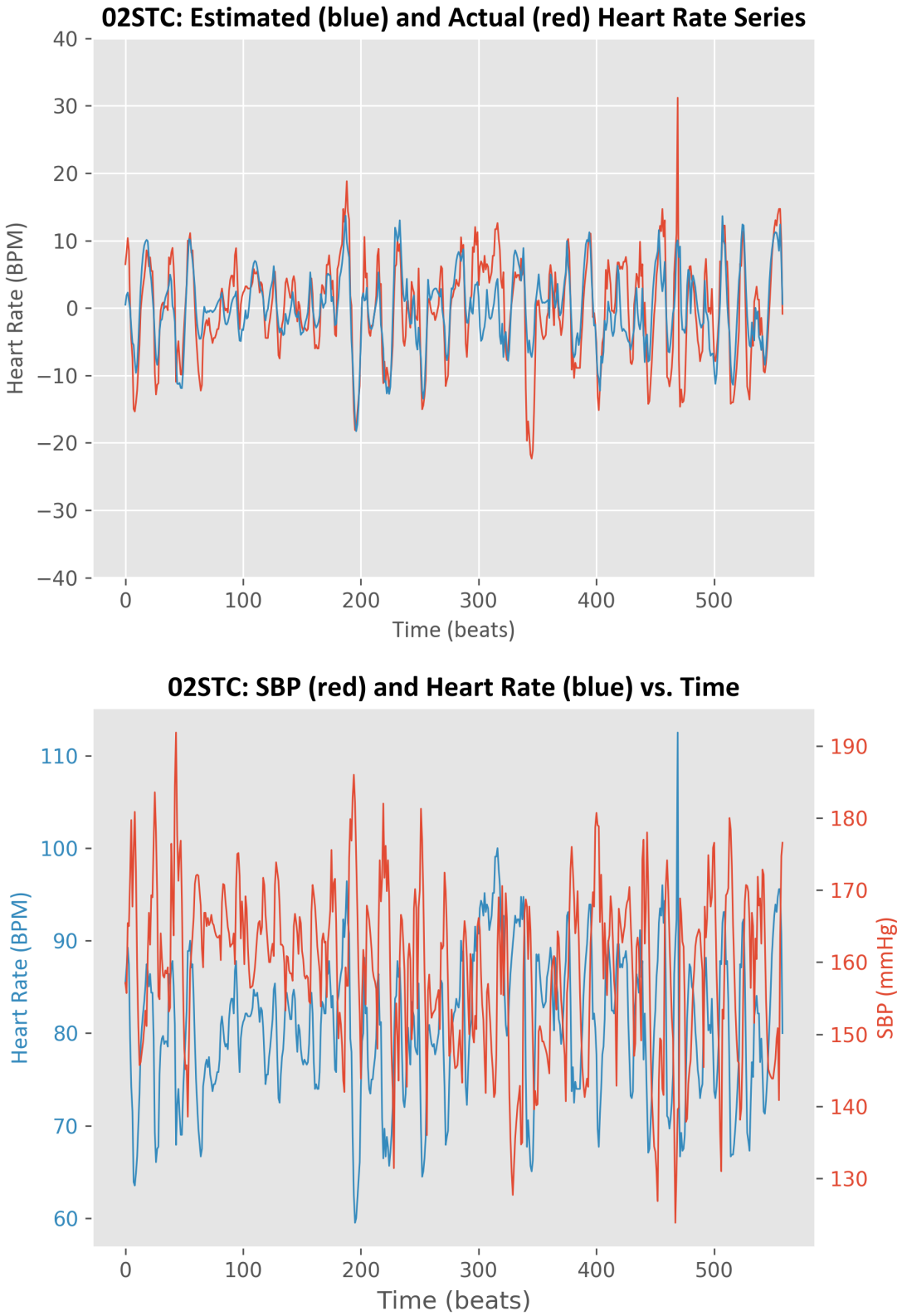

FIGURE 4.5: Estimated and actual HR time series for 02STC (top), and actual HR and SBP time series for 02STC (bottom). Note that 02STC coheres well with our model assumptions as the SBP and true HR signals are almost completely 180° out of phase with each other. This manifests in close estimation of the HR time series.

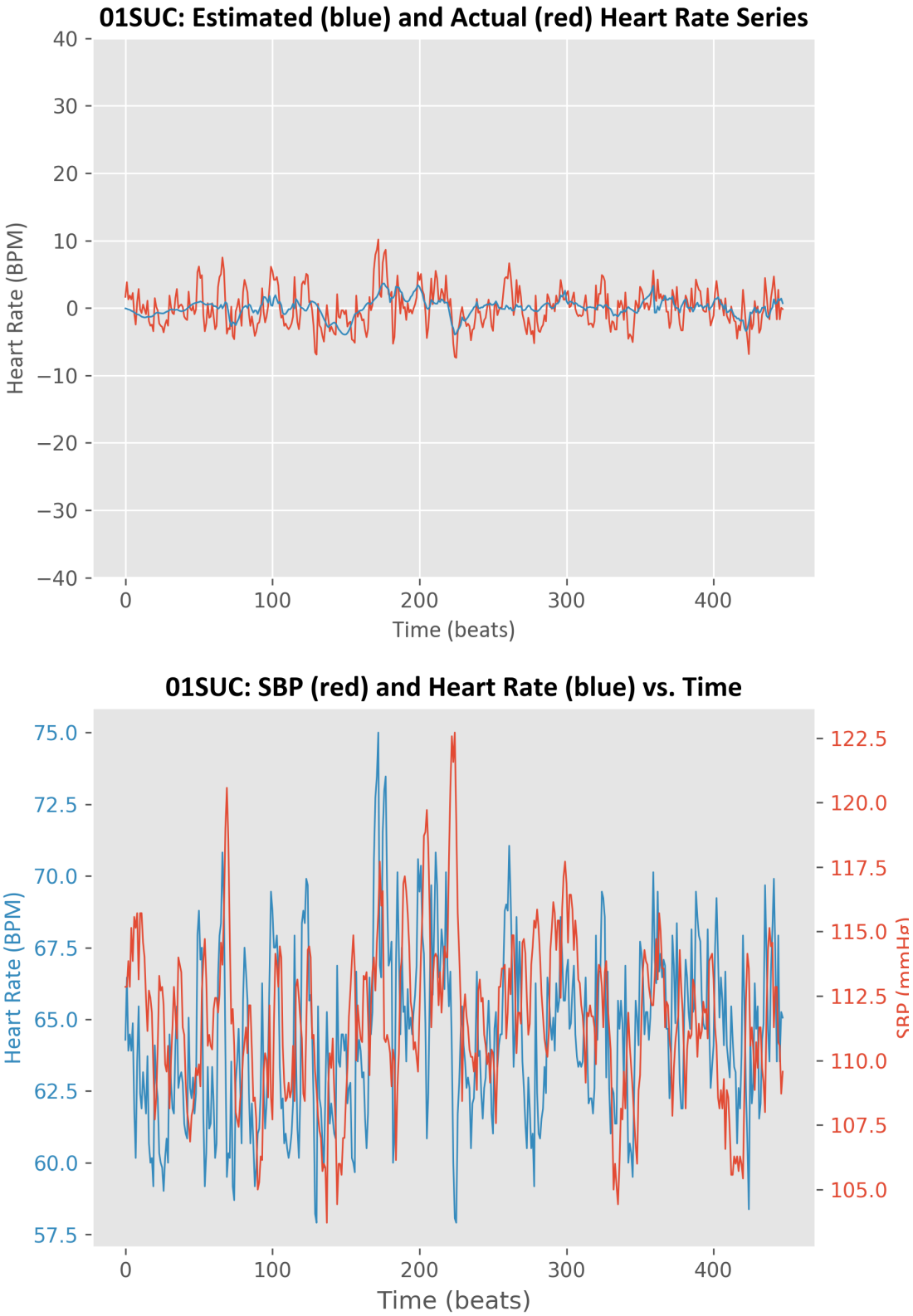

FIGURE 4.6: Estimated and actual HR time series for 01SUC (top), and actual HR and SBP time series for 01SUC (bottom). 01SUC does not cohere well with our model assumptions as the SBP and true HR signals are inconsistently out of phase with each other. This manifests in poor estimation of the HR time series.

4.3.1 Results

In the absence of pharmacological blocking agents, the parasympathetic-sympathetic ratio (PSR)[1] was depressed in ten out of twelve subjects after subjects shifted from the supine to standing position (Figure 4.7). As posture changes from supine to standing, sympathetic outflow should increase and parasympathetic outflow should decrease, resulting in a decrease in PSR. The estimated PSRs closely track this expected decrease in PSR as a result of changing posture, with a mean change of -0.25 ± 0.23 n.u.[2]

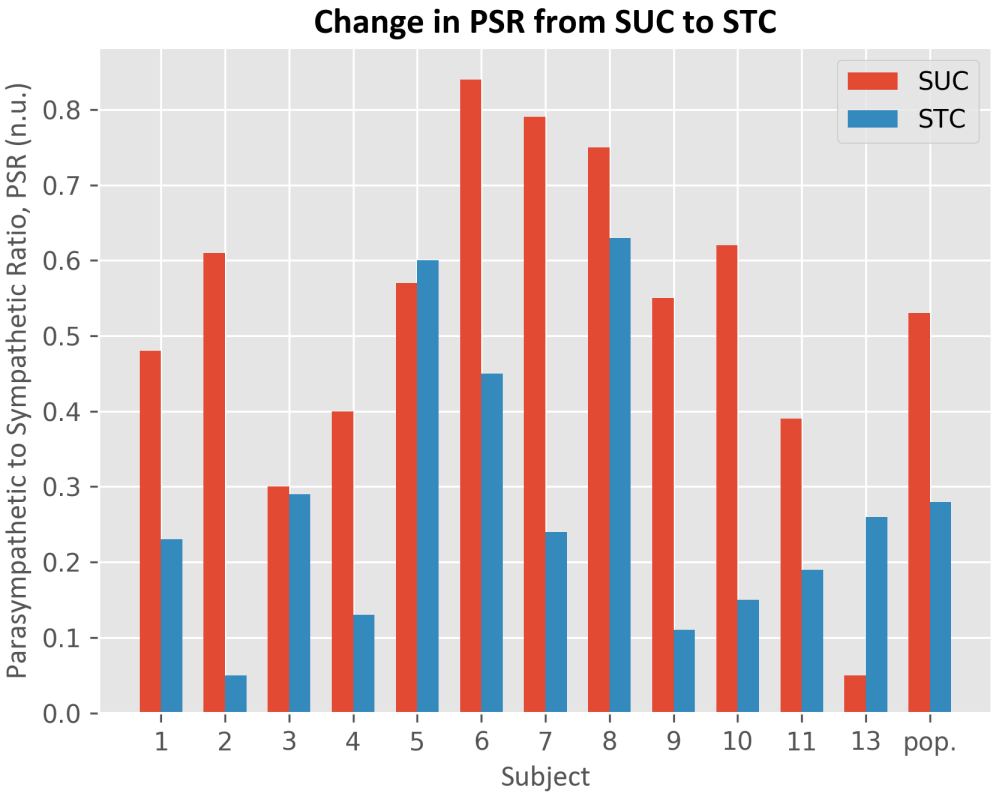

FIGURE 4.7: Plot of PSR in the SUC and STC states for twelve subjects. Subject 12 is excluded, as there were no windows that fit the acceptance criterion.

Likewise, expected changes in autonomic balance resulting from pharmacological blockade are well tracked by both the estimated PSRs and by the estimated parameter

[1] For convenience, the formula for PSR from Section 3.4 is reproduced here: $PSR = \frac{K_p}{K_p + K_s/(1-\beta)^2}$

[2] Normalized units

values themselves. In the case of sympathetic blockade, we expect PSR to increase and K_s to decrease in magnitude after the administration of propranolol. In the case of parasympathetic blockade, however, we expect both the PSR and K_p to decrease after the administration of atropine.

The administration of propranolol resulted in categorical increases in PSR with a mean change of 0.34±0.20 n.u, and decreases in the magnitude of sympathetic gain, K_s (Figure 4.8). The administration of atropine yielded categorical decreases in the magnitude of the parasympathetic gain, K_p, and ambiguously altered PSR with a mean change of 0.07±0.40 n.u. (Figure 4.9). Though the K_p magnitudes decreased in all subjects, in some subjects K_p became positive. More generally, K_p became less negative in all subjects due to parasympathetic blockade.

The ambiguity in changes to PSR as a result of parasympathetic blockade is likely a consequence of the lack of resolution in the HR time series, which makes it difficult to estimate parameters accurately. In particular, atropine's affect in reducing HRV manifests in some of the SUA recordings as a reduction in the range of RRI values to as low as 10ms, which in signals sampled at 360Hz yields only 4 possible RRI values (and thus only 4 possible HR values), whereas the variability in the SBP signal can yield hundreds of SBP values. While the model is unable to accurately estimate parameters in the case of strongly inhibited parasympathetic activity, HRV is sufficient in classifying these cases, and obviates the need for the model.

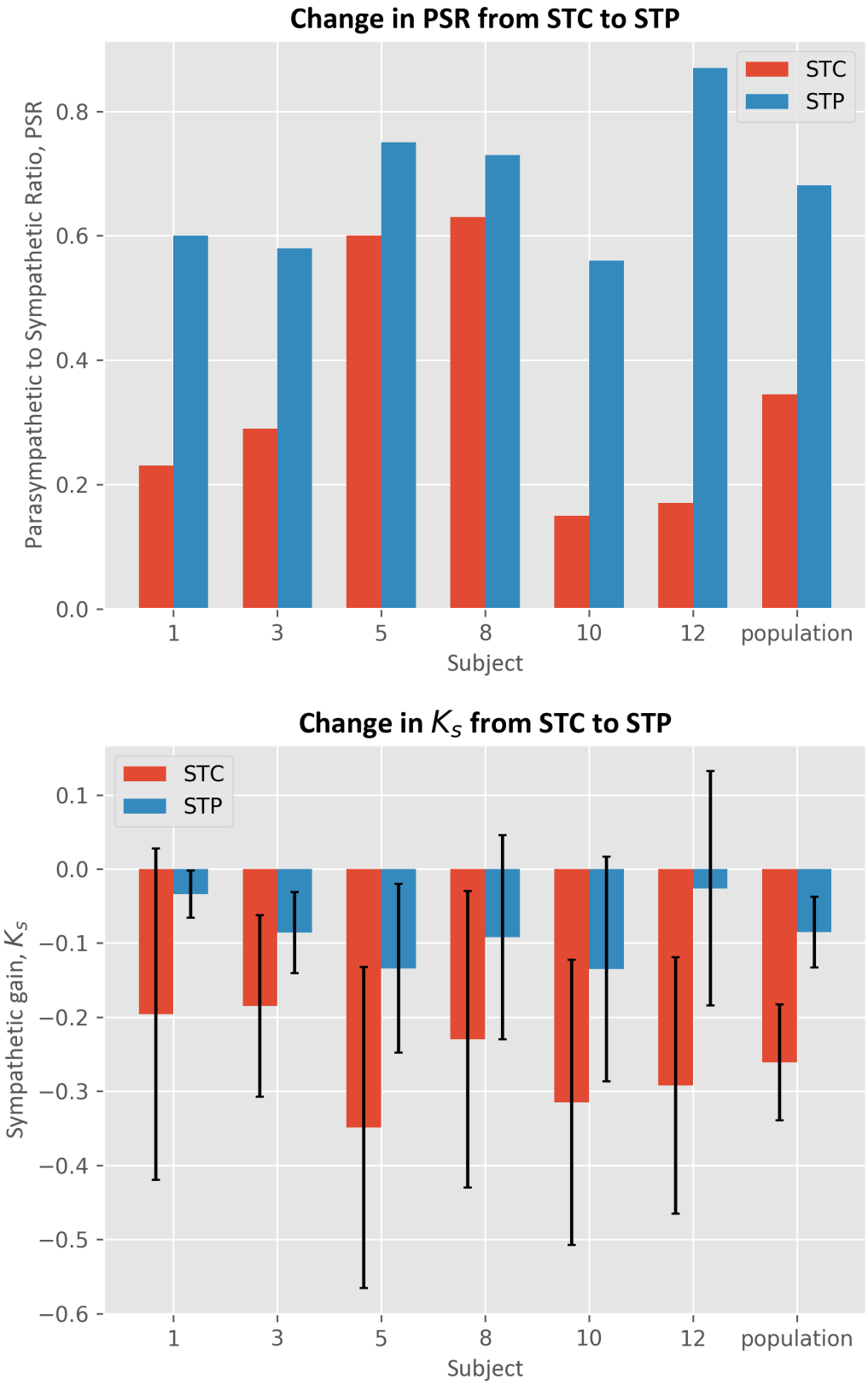

FIGURE 4.8: Comparison of PSR between the STC and STP recordings (top), and comparison of K_s between the STC and STP recordings (bottom). Figure shows means (bars) and standard deviations (error bars).

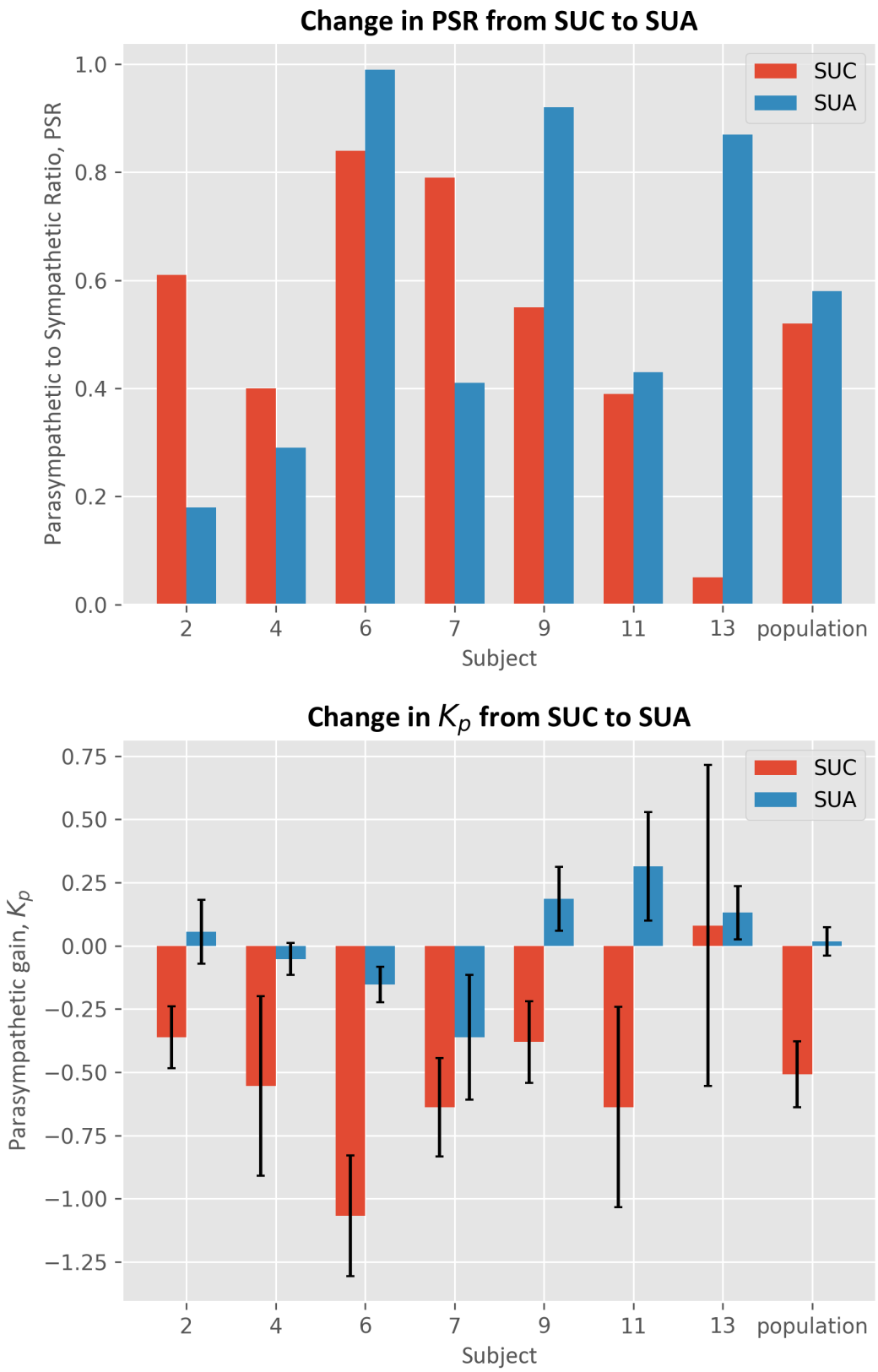

FIGURE 4.9: Comparison of PSR between the SUC and SUA recordings (top), and comparison of K_p between the SUC and SUA recordings (bottom). Figure shows means (bars) and standard deviations (error bars).

Finally, as the number of taps in the parasympathetic model impulse response increased, the RMSE between the true and estimated HR time series decreased (Figure 4.10).

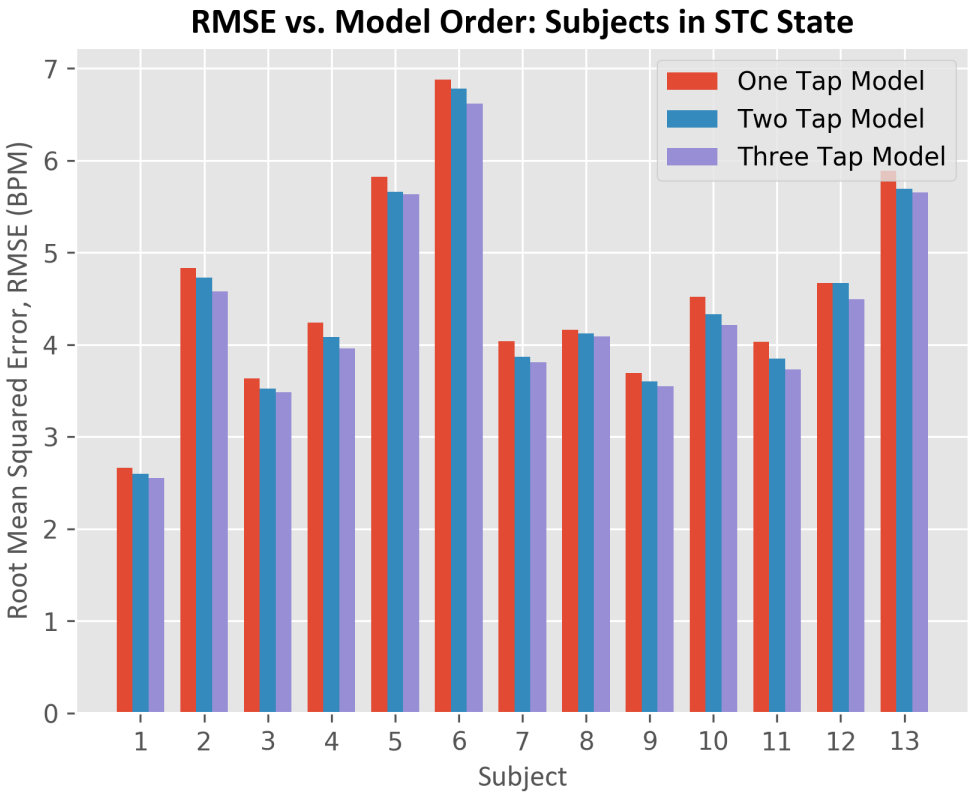

FIGURE 4.10: Graphical comparison of decreasing RMSE as taps increase. 14STC is one of the five missing records, hence its exclusion from this graph.

While increasing the number of taps in the parasympathetic impulse response results in better minimization of the estimation error, using greater than one tap appears unwarranted due to two reasons. First, the improvement in error is rather modest, as shown in Figure 4.10 with the standing control cases, and the improvement primarily occurs in windows in which the model already conforms well to the data. Second, parasympathetic impulse responses with greater than one tap are difficult to explain physiologically, especially as the parameter estimates (including the sympathetic gain, K_s) vary widely within each subject-state record. While the application of regularization

to the estimation problem may reduce the variance of the parameter estimates, it would necessarily result in an increase in error over the non-regularized estimation, and reduce the already modest improvement in error with respect to the one tap model.

4.3.2 Discussion

By visual inspection, our model comports with the data for some of the subject-states, such as subject-state 02STC, and does not comport with the data for other subject-states, such as subject-state 01SUC. For windows within a subject-state for which the model does not fit well to the data, visual inspection of plots of SBP and HR superimposed, such as Figures 4.5-4.6, provide clarity. In particular, as noted in Section 3.1, the structure of the model assumes that RRI and SBP covary, or in terms of the system variables, that SBP and HR vary in opposite direction. For windows in which the data adhere to that assumption, the model performs very well, as shown in Figure 4.5, whereas for windows where the data do not adhere to that assumption, the model performs poorly, as shown in Figure 4.6. For windows with poor model fit, however, the estimated heart rate typically exhibits less variation relative to the true heart rate and is rather flat in shape, which is a result of the optimization algorithm preventing error accumulation due to estimation overshooting. Including parameter estimates from such windows in the parameter ensembles is imprudent, and their removal from the pharmacological blockade dataset resulted in either no change or lower variance in parameter estimates across most subject-state recordings.

The mean parameter values for each subject-state tracked well with the expected change in autonomic balance, illustrated in Figures 4.7-4.9. Moreover, the standard

deviations of the parameter ensembles were smaller than changes in the means of the parameter ensembles due to a change in state for a single subject. Nevertheless, there are remaining questions regarding the stability of the parameter estimates. In the cases of subject-states with parameter ensembles exhibiting significant window-to-window variability, this may be a result of significant noise or highly time varying properties of the baroreflex. Sensitivity analysis will be performed in Chapter 7 to determine the effects of noise on the parameter estimation.

The observation of positive values of K_p while subjects were under parasympathetic blockade suggests that K_p may be capturing some of the mechanical respiratory contributions to heart rate, that K_p acts as a free parameter that fits to noise when parasympathetic activity is severely inhibited, or some combination thereof [32,37]. Filtering out heart rate variations due to high frequency respiratory fluctuations could potentially reduce error due to respiratory influences, and prevent estimates of K_p from becoming positive. Such filtering may prove to be difficult since the beat series cannot be uniformly sampled in the time domain if there is any heart rate variability. Without this filtering, it appears that as the parasympathetic nervous system is increasingly inhibited, we should expect K_p to become less negative, and not necessarily that its magnitude decrease.

Overall, while the open-loop model performs well in fitting much of the data and providing evaluations of autonomic balance, there are a few deficiencies. One deficiency is that the estimated HR series for many windows, even windows that cohere well to the model assumptions, cannot fit to some of the sharp features of the actual HR series. Another deficiency is that the variances of the estimated parameters are large in some

cases, raising doubts as to the model's accuracy and assumptions. One possible remedy for these flaws is closing the loop, which should more accurately model the closed-loop nature of the baroreflex as opposed to the open-loop model. In the proceeding chapters, we shall explore a parameterized closed-loop model of baroreflex further.

To conclude this chapter, we will discuss the differences between the transfer function method (TF) and the parameterized model-based method (PM). The primary difference between the two models is that the TF appears to only be sensitive to parasympathetic changes, while the PM appears to be sensitive to both parasympathetic and sympathetic changes. Moreover, the PM provides greater interpretability than the TF as it separates the gains of the parasympathetic and sympathetic branches through K_p and K_s, respectively, while the TF provides one value, the BRS, increasing the difficulty of determining autonomic balance. Despite the clear advantages of the PM in this analysis, it is difficult to know which method is more sensitive to aggregate autonomic without some gold standard measurement for comparison.

Chapter 5

Closed-loop Modeling of the Baroreflex

The limitations of transfer function analysis and our open-loop model from the prior chapters motivate this chapter. First, because the baroreflex is naturally closed-loop, the open-loop model is by default incorrect, and ultimately inadequate in explaining some of the observed phenomena in the blood pressure such as Mayer waves. Some features of the heart rate waveform, such as the sharpness of the oscillations, may potentially be better fit with a closed-loop model as opposed to the open-loop model from Chapter 3. Second, while baroreflex sensitivity as determined by the transfer function method yields an overall assessment of the heart rate arc of the baroreflex, it does not provide specific information regarding autonomic balance. Thus, the goal of this chapter is to develop a robust parameterized model that addresses these concerns.

5.1 Closed-loop Framework

To address the first concern from the Introduction, we present a closed-loop model of the baroreflex. Significant prior work has been done in closed-loop modeling of the baroreflex. Akselrod *et al.* modeled the closed-loop system coupling heart rate (HR) to arterial blood pressure (ABP) as the combination of a forward baroreflex arc, transforming ABP to HR, and a backward mechanical arc, transforming HR to ABP [10]. Both the forward and backward arcs of the control loop were considered LTI systems, which resulted in the computation of nonparametric linear transfer functions between the variables of interest for analysis. Appel expanded Akselrod's model to explicitly include respiratory contributions to blood pressure (with processing of the instantaneous lung volume signal), and then parameterized the system using an autoregressive-moving-average model [38]. Finally, Saul *et al.* developed a parameterized closed-loop model based on physiological insight that parameterized the responses of the sympathetic and parasympathetic branches as first-order low-pass filters [32].

The canonical feedback control system[1] with a controller, plant, and sensor, as shown in Figure 5.1, is the basis for our model. Direct analogies for the controller, plant, and sensor, in the baroreflex control loop are the autonomic nervous system, the cardiovascular system, and the baroreceptors, respectively.

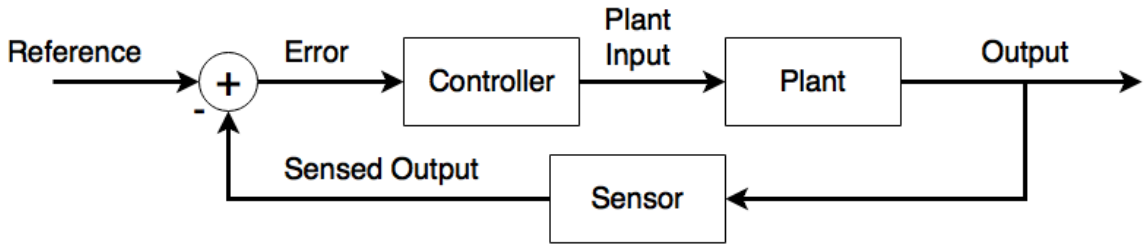

Figure 5.1: Canonical negative feedback control system.

[1] In this chapter, we use the terms *feedback* and *closed-loop* interchangeably.

In terms of system variables, the plant input, plant output, sensed output and reference correspond to the heart rate (HR), systolic blood pressure (SBP), baroreceptor pressure, and the baroreflex blood pressure set point, respectively. The closed-loop system model for the heart rate arc of the baroreflex is shown in Figure 5.2.

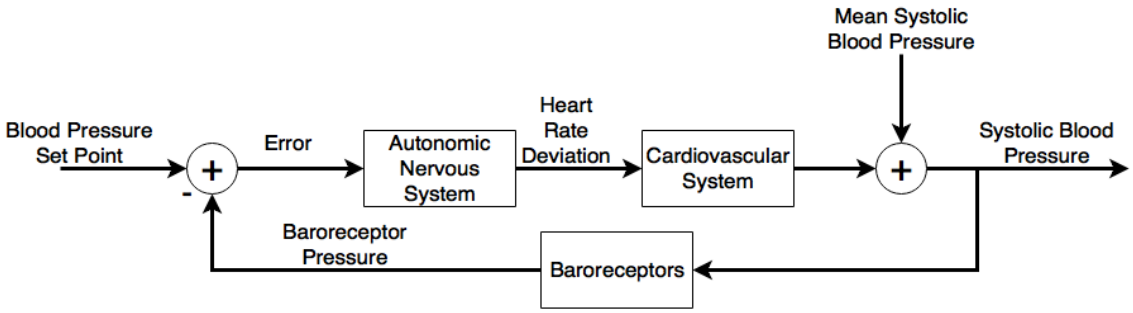

Figure 5.2: Block diagram of the heart rate baroreflex feedback loop.

5.2 Parameterization

To address the second concern from the Introduction, we shall explicitly parameterize each of the blocks in our system model from Figure 5.2. In concordance with our parameterized open-loop model, our closed-loop model is also beat-to-beat, and acting on the demeaned beat series.

5.2.1 Baroreceptors (sensor)

The time scale of the response of baroreceptors to changes in blood pressure was demonstrated by Eckberg to be approximately 0.25 seconds, while a conservative lower bound for heartbeat length in a resting patient is 0.4 seconds [39]. With our beat-to-beat model, we make the assumption that beat length is greater than the time scale of the baroreceptors response to changes in blood pressure. We therefore model the baroreceptor block as a unity gain, implying that at each time step the systolic blood pressure and the pressure sensed by the baroreceptors are identical.

5.2.2 Autonomic Nervous System (controller)

We model the autonomic nervous system block in the closed-loop model identically to that of the open-loop model presented in Section 3.4:

$$H_{Baroreflex}(z) = K_p + \frac{K_s z^{-1}}{(1-\beta z^{-1})^2} \tag{5.1}$$

Where K_p represents the parasympathetic gain, K_s the sympathetic gain, and β the characteristic time constant of the sympathetic nervous response. In Chapter 4 it was shown that increasing the number of taps in the impulse response of the parasympathetic branch does not dramatically improve the fit of the model. We thus use a single-tap impulse response to represent the parasympathetic response in order to preserve parsimony.

5.2.3 Cardiovascular System (plant)

The cardiovascular system is modeled as a gain delayed by one beat. Our single-step delay element models the latency between decision making at the output of the autonomic nervous system, and action at the output of the cardiovascular system [32]. This latency was demonstrated by Berger to be approximately 0.42 seconds, which is slightly larger than the conservative lower bound for heart beat length of 0.4 seconds given in Section 5.2.1 [40].

In Chapter 2, we established that mean arterial blood pressure is the product of heart rate, stroke volume, and total peripheral resistance. It follows that the gain is the product of stroke volume and total peripheral resistance. Using standard values for stroke volume (70 cc) and total peripheral resistance (1500 dyne-s/cm^5) yields a gain on the

order of 1 mmHg/BPM [2]. For simplicity, we assume that the gain is constant in time, and is represented by the parameter K_c.

5.2.4 Full Model

Now that we have parameterized all the blocks, we can assemble the full control loop as shown in Figure 5.3. Since the model requires the signals to be demeaned around the operating point, our blood pressure set point (reference) is set to zero. In addition, for notational clarity we prepend lowercase "d" to each of the signal names, indicating deviation from mean value.

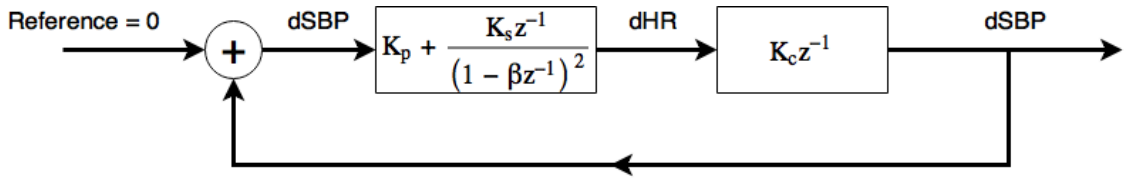

Figure 5.3: Fully parameterized closed loop model of baroreflex.

5.3 Noise

While it is very difficult to model noise in the system *a priori*, it is instructive to consider what sources of noise exist, what parts of the model they affect, and how to potentially counter their effects when estimating model parameters. In our model, sources of noise primarily manifest at the output of the cardiovascular block, shown in Figure 5.4.

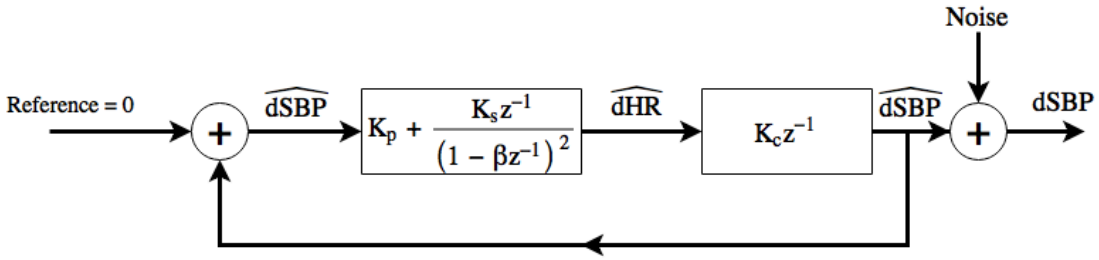

Figure 5.4: Closed loop model in the presence of noise. Hat notation implies estimate, i.e. $\widehat{dHR}$ is an estimate of the true value of dHR, and $\widehat{dSBP}$ is an estimate of the true value of dSBP.

5.3.1 Sources

One main source of noise comes from the simplicity of our model (modeling error). Chiefly, because only the heart rate arc of baroreflex is modeled, the model cannot predict changes in systolic blood pressure (SBP) accounted for by beat-to-beat changes in cardiac contractility and vascular tone. For example, both stroke volume and total peripheral resistance vary in time on a beat-to-beat basis, making K_c beat dependent and rendering the cardiovascular system block time variant. Hence, the addition of noise is exhibited at the output of the cardiovascular block due to the inability of the time invariant model to capture the time varying behavior.

Another source of noise, though smaller, is the mechanical coupling between respiration and the thoracic vasculature. This, too, is a time varying phenomena affecting the cardiovascular block, and cannot be modeled in a time invariant manner in the absence of a respiratory signal [39].

5.3.2 Error Compensation

Unlike in the case of the open-loop model, signal estimation errors can propagate through the feedback loop and may lead to significant errors when attempting to estimate model parameters (as we shall see in Chapter 6). A major task is preventing divergence of system estimates due to feedback of an incorrect estimate. This can be accomplished by compensating for the error at each step with the system in Figure 5.5. In this system, the input to the ANS block at every time step is a weighted combination of the estimated output from the prior time step, $\widehat{dSBP}$, and the true output, dSBP. This reduces how far an input at any time *n+1* will stray from the true output at time *n*. Additionally, if we set

the output and input weights to be γ, and $1-\gamma$, respectively, where $0 < \gamma < 1$, then while errors will still occur, they are discounted by a factor of $1-\gamma$ for every cycle through the loop. For γ chosen sufficiently small, the model maintains its closed-loop character, while simultaneously not diverging too far in its estimation. In the limit where γ approaches 1, the model is identical to the pure closed-loop model presented in Section 5.2.4.

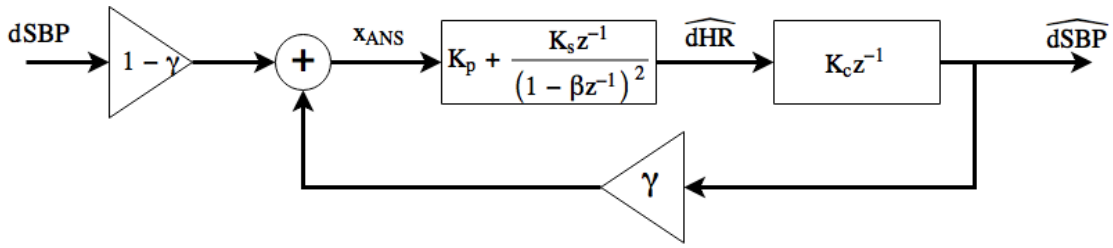

Figure 5.5: Updated control loop with error compensation.

Chapter 6

Closed-loop Model Analysis

In this chapter, we analyze the performance of the two closed-loop models[1] defined in Chapter 5. We first estimate parameters for the closed-loop models using an optimization formulation similar to that from Section 4.3 and the same dataset. With these parameters, we then analyze the ability of the closed-loop models to track the expected physiological changes in the subjects from the dataset. Finally, we consider the effect that closing the loop has on parameter estimation with respect to the open-loop model parameter estimates.

6.1 Closed-loop Parameter Estimation

Closed-loop parameter estimation presents new challenges beyond the formulation for open-loop parameter estimation given in Section 4.3. While our error criterion and optimization method remain the same, our parameter space has grown with the addition

[1] For convenience, we will use the abbreviations *CLM* for the standard closed loop model from Section 5.2.4 and *CLECM* for the closed loop error compensated model from Section 5.3.2

of the cardiac parameter K_c. In the closed loop parameter estimation we now have an updated collection of system parameters:

$$\vec{\theta} = \begin{bmatrix} K_p & K_s & \beta & K_c \end{bmatrix} \tag{6.1}$$

but the same objective function as in the open-loop case:

$$\vec{\theta}_{min} = \underset{\vec{\theta}}{\operatorname{argmin}} \left\| \overrightarrow{HR} - \widehat{\overrightarrow{HR}}(\vec{\theta}) \right\|_2 \tag{6.2}$$

As opposed to the open-loop model, the closed-loop models are not fed a continuous stream of inputs of the true systolic blood pressure (SBP) into the autonomic nervous system (ANS) block at each time step (beat). We therefore adjust our simulation method by providing initial conditions to drive the system. Specifically, we set the input to the ANS at time step $n = 0$ to be the true value of SBP at the beginning of the data window. In the CLM case, an estimate of SBP at the output of the cardiovascular system (CVS) block at each beat is fed as the input to the ANS block of the following beat. Similarly, in the CLECM case, a weighted sum of the estimated SBP at the output of the CVS block and true SBP at each time step is fed as the input to the ANS block. By recognizing that the CLM is a special case of the CLECM where $\gamma = 1$, the time evolution of both of the models may be simulated identically. Finally, to prevent divergence of our parameter estimates from physiological limits, we bound our parameter estimation to conservative approximations of those limits given below

$$K_P \, \epsilon \, \Big(-3, 3\Big); \quad K_S \, \epsilon \, \Big(-3, 3\Big); \quad \beta \, \epsilon \, \Big(0, 1\Big); \quad K_C \, \epsilon \, \Big(-3, 3\Big) \tag{6.3}$$

with units of $\frac{bpm}{mmHg}$, $\frac{bpm}{(beat)*(mmHg)}$, $\frac{1}{beat}$, and $\frac{mmHg}{bpm}$ respectively [29].

Using the estimation problem given by Equation 6.2, we performed windowed parameter estimation for the CLM and CLECM (with $\gamma = 0.5$) on each of the seventy-

nine subject-state recordings. Parameter ensembles for each subject-state were saved, and the mean and variance of each parameter ensemble were computed.

Just as in the open-loop case, we excluded parameters in our parameter ensembles from windows where the model did not cohere well with the model assumptions, using the criterion given by Equation 4.4. For the CLM, 82 out of a total 787 windows (over the 83 recordings) were excluded, and in terms of subject-states, 37 out of the 83 subject-state recordings had windows excluded. For the CLECM, 68 out of a total 787 windows (over the 83 recordings) were excluded, and in terms of subject-states, 42 out of the 83 subject-state recordings had windows excluded.

6.2 Results

Both the CLM and CLECM were unable to track postural changes in the absence of pharmacological blockading agents. The CLM computed parasympathetic-sympathetic ratio (PSR) was depressed in five of thirteen subjects with a mean change of 0.07 ± 0.29 n.u.[2] after subjects shifted from the supine to the standing position (Figure 6.1). Similarly, the CLECM computed PSR was depressed in eight of thirteen subjects with a mean change of -0.07 ± 0.37 n.u. (Figure 6.1). Neither of the two models exhibit a consistent decrease in PSR, which is in contrast to the physiological expectation that sympathetic outflow increase and parasympathetic outflow decrease as posture shifts from the supine to standing position.

With regards to the expected changes in autonomic balance due to pharmacological blockade, the CLM was unable to track such changes while the CLECM

[2] normalized units

was able to track such changes, though with low fidelity. Neither the administration of propranolol nor the administration of atropine resulted in any discernible trends in PSR, K_p, or K_s given the CLM, as any changes in parameter values were well within the error of the parameter estimation for all subjects (Figures 6.2, 6.3). For the CLECM, the administration of propranolol yielded no discernible trend in PSR, and resulted in K_s becoming less negative in five of the six subjects, though most of these changes were within the error of the parameter estimation (Figure 6.4). This does not comport with the physiological expectation that PSR increases, and K_s decrease in magnitude. The administration of atropine also yielded no discernible trend in PSR for the CLECM, but did result in K_p becoming more positive in all seven of the subjects, with a population change outside the margin of error of the parameter estimation (Figure 6.5). This observed change is in agreement with the physiological expectation that PSR increase, and K_p decrease in magnitude.

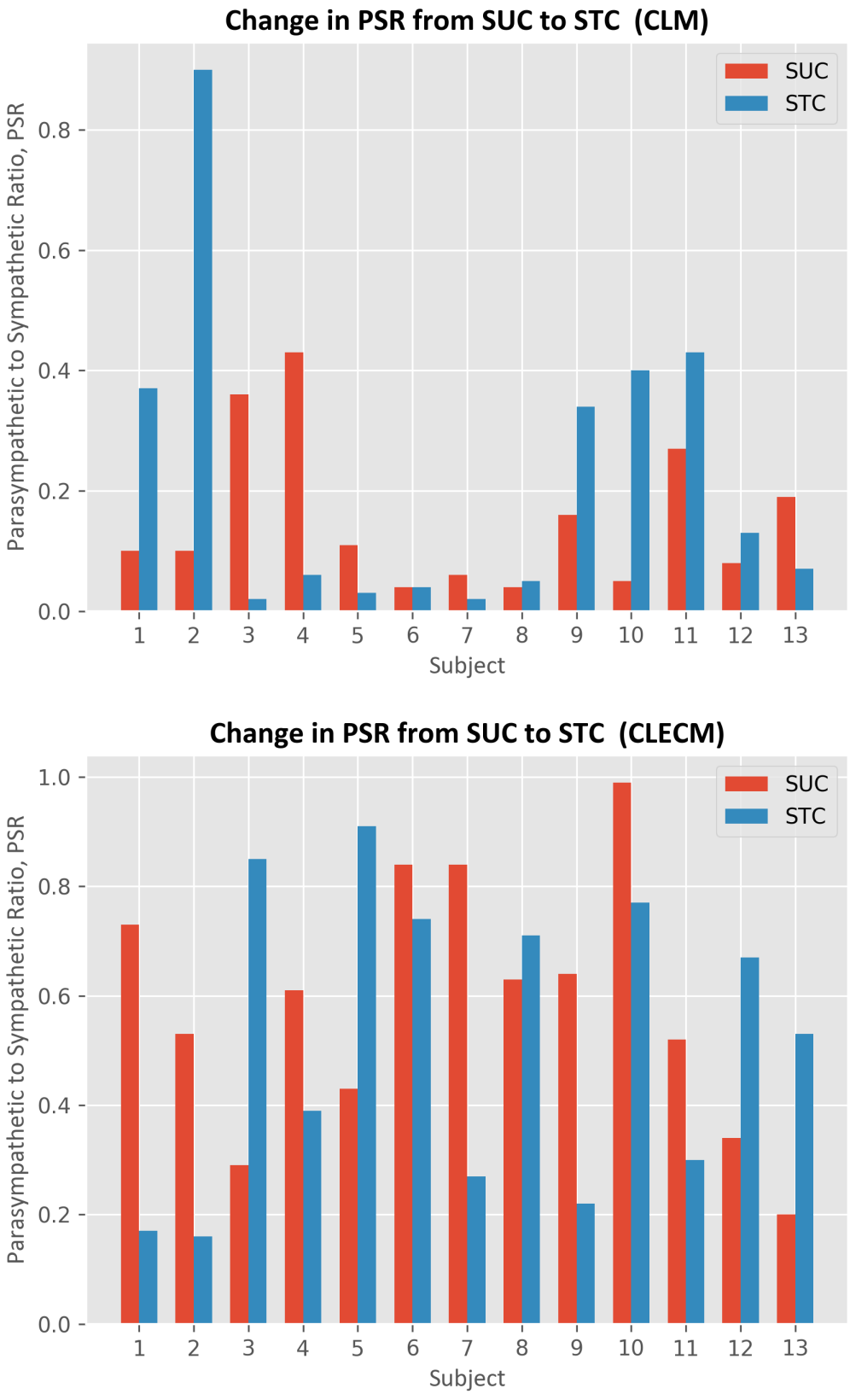

FIGURE 6.1: Plot of PSR in the SUC and STC states for thirteen subjects computed given CLM model (top) and CLECM model (bottom).

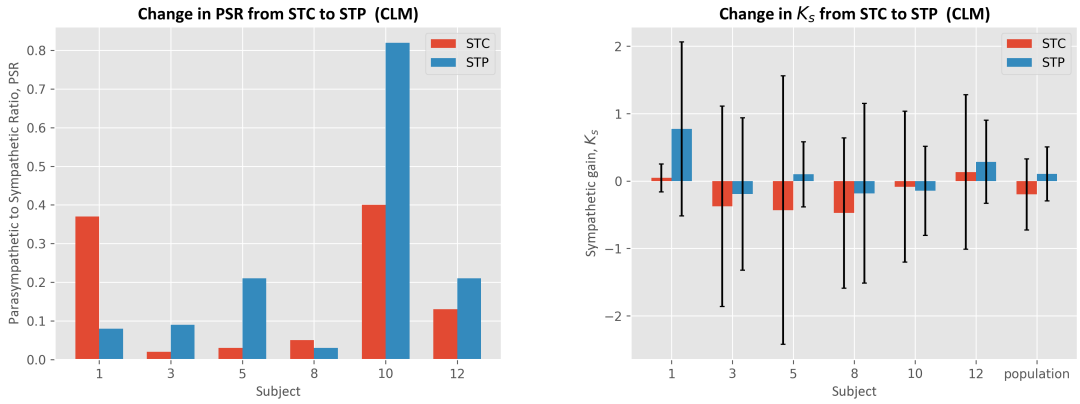

FIGURE 6.2: For the CLM, comparison of PSR between the STC and STP recordings (left), and comparison of K_s between the SUC and SUA recordings (right).

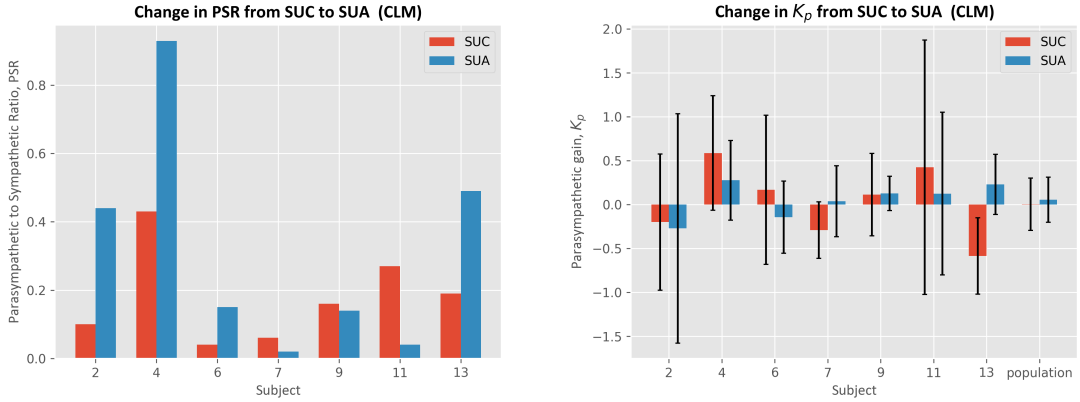

FIGURE 6.3: For the CLM, comparison of PSR between the SUC and SUA recordings (left), and comparison of K_p between the SUC and SUA recordings (right).

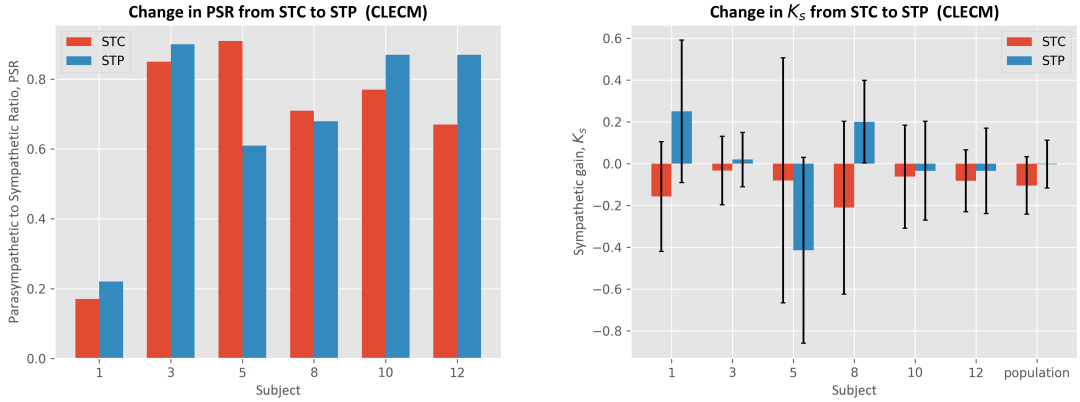

FIGURE 6.4: For the CLECM, comparison of PSR between the STC and STP recordings (left), and comparison of K_s between the SUC and SUA recordings (right).

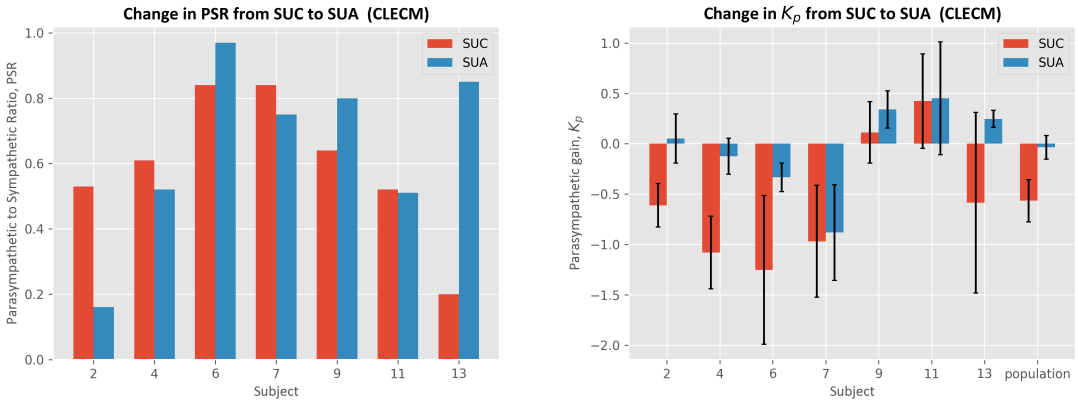

FIGURE 6.5: For the CLECM, comparison of PSR between the SUC and SUA recordings (left), and comparison of K_p between the SUC and SUA recordings (right).

6.3 Discussion

Whereas the open-loop model effectively tracked changes in autonomic balance, the closed-loop models surprisingly did not. Combining the results of this chapter with the results from Chapter 4, a clear relationship emerges between a model's ability to track changes in autonomic balance and whether or not it is open or closed loop. In particular, we find that as the model becomes more closed in character, i.e. the strength of the feedforward arm of the control loop decreases relative to the strength of the feedback arm of the control loop, the variance of the parameter estimates increases, while the parameters no longer track the physiological changes. A naïve interpretation of this relationship is that closed-loop models are less accurate models of the baroreflex than open-loop models. It appears, however, that closed-loop models are not less accurate models, rather that model error due to only considering the heart-rate arc of the baroreflex accumulates when closing the loop, which leads to aberrant parameter estimates. Model noise does not affect the open-loop model as significantly as the closed-loop models since the input at each beat is the true SBP, which prevents error accumulation and propagation over time. Lastly, it is important to note that the CLM

places implicit conditions on the poles of the system. The system is undriven beyond its initial conditions, which requires that at least one system pole have a magnitude very close to unity such that there is no runaway decay of the output, and that no pole has a magnitude larger than unity in order to prevent runaway growth of the output.

Chapter 7

Closed-loop Model Analysis

In Chapter 4 we demonstrated that model parameters of an open-loop model for baroreflex were able to accurately track changes in autonomic balance. We motivate this chapter by considering how those model parameters are obtained, and how large the effect size is with regards to changes in autonomic balance. In Section 7.1 we present a method for testing the sensitivity of our parameter estimates to perturbations in the inputs to our parameter estimation. We then execute this method on the same dataset used in Chapter 4, and evaluate the sensitivity of our model in Section 7.2.

7.1 Methods

Our criterion of success for the open-loop model was if it could correctly detect changes in autonomic balance. In particular, we tested whether or not certain model parameters changed in an expected direction after a subject switched between two states of differing autonomic activity (supine to standing, parasympathetic blockade, sympathetic blockade). Accordingly, in this sensitivity analysis, our first evaluation criterion is how

well the model parameters are able to track their expected changes when the inputs to the parameter estimation algorithm are perturbed. Our second evaluation criterion is how greatly do the parameter estimates themselves change between the unperturbed and perturbed parameter estimation, and whether the new parameters maintain physiological relevance and meaning. In the presence of noise, the first criterion measures the model's precision while the second criterion measures its accuracy. In the following section, will will evaluate these criteria qualitatively.

With our evaluative criteria defined, we now move on to our perturbation method. Given a subject-state (as defined in Chapter 4), we perturb either $\overrightarrow{SBP}$ or $\overrightarrow{HR}$ with some well defined level of noise before performing parameter estimation on the open-loop model (for notational convenience, we denote the perturbed signals with a subscript p, *i.e.* $\overrightarrow{SBP_p}$ and $\overrightarrow{HR_p}$). Specifically, the parameter estimation algorithm either feeds $\overrightarrow{SBP_p}$ as the input into the open-loop model while fitting the output to $\overrightarrow{HR}$, or it feeds $\overrightarrow{SBP}$ as the input into the open-loop model while fitting the output to $\overrightarrow{HR_p}$. In this analysis, we perturb the signals with additive white Gaussian noise (AWGN), as AWGN is zero-mean in the time domain, and has a uniform power spectrum in the frequency domain [41]. Mathematically our perturbed signal is:

$$\vec{X}_p = \vec{X} + \vec{Z} \tag{7.1}$$

Where the elements of $\vec{Z}$ are samples independently and identically distributed from a Gaussian distribution with a mean of zero and a variance of σ^2, defined as:

$$\sigma^2 = \alpha * var(\vec{X}), \tag{7.2}$$

In this structure, the variance of the perturbation signal is just some proportion, α, of the variance of the input signal, $\vec{X}$. Thus, setting α and determining which signal to perturb ($\overrightarrow{SBP}$ or $\overrightarrow{HR}$) defines the perturbation scheme.

Using the same dataset, parameter estimation formulation, and parameter inclusion criteria as in Section 4.3, we tested four perturbation schemes summarized in Table 7.1, running each scheme once per subject-state.

Perturbation Scheme	$\vec{X}$	α	Number of Windows Excluded	Number of Effected Subject-states
A	$\overrightarrow{SBP}$	0.05	137	60
B	$\overrightarrow{SBP}$	0.10	151	64
C	$\overrightarrow{HR}$	0.05	143	59
D	$\overrightarrow{HR}$	0.10	159	63
Control	Neither	0	135	57

Table 7.1: Summary of perturbation schemes. In all four schemes (A-D), parameters were estimated for 787 distinct windows. The bottom row labeled "control" represents the unperturbed open loop parameter estimation performed in Chapter 4.

7.2 Results

The combination of the open-loop model and parameter estimation formulation from Chapter 4 appears to be rather robust in the presence of low noise (5% and 10% signal variance in our schemes). All four perturbations schemes performed as well as the unperturbed parameter estimation in tracking the change in autonomic balance due to postural changes (Figure 7.1).

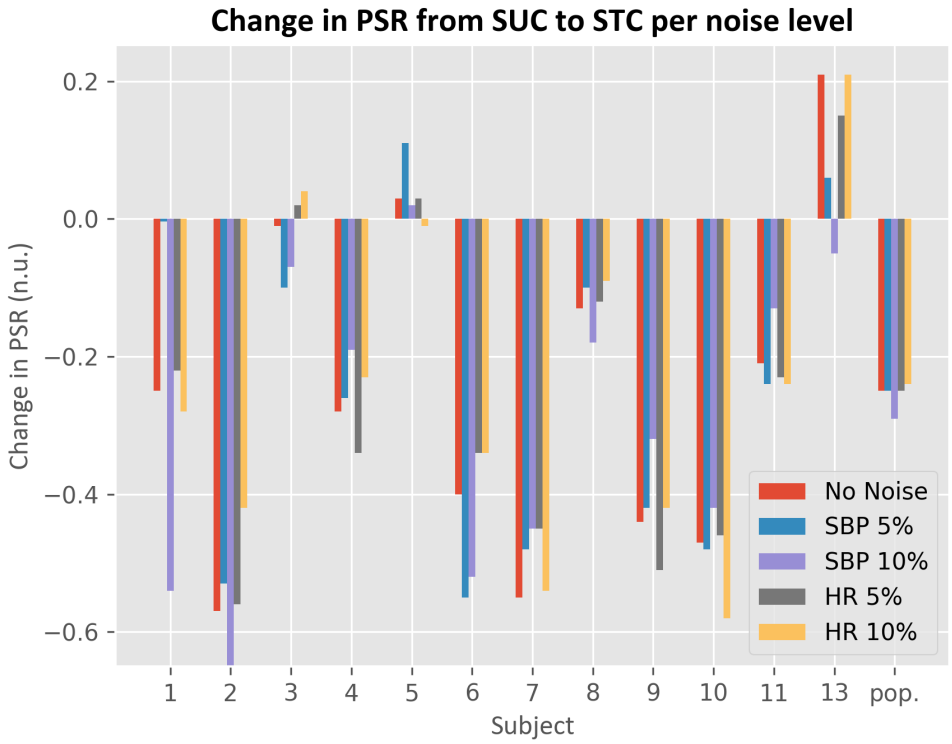

Figure 7.1: Changes in PSR from SUC to STC for each perturbation scheme. The "No Noise" scheme is the original set of estimates. Population mean is represented by the subject "pop."

In consonance with this result, the four perturbation schemes also performed as well as the unperturbed parameter estimation in tracking the change in autonomic balance caused by pharmacological blockade (Figure 7.2). From these results, it is clear the model satisfies the first criterion, *i.e.* tracking the relative shifts in autonomic balance, at the levels of noise injected into the system. The model also appears to satisfy the second evaluation criteria, the amount that the estimated parameters changed from the unperturbed scheme to the perturbed schemes. Visually, it is clear from Figure 7.3 that the estimated parameters of the perturbed systems do not significantly deviate from the estimated parameters of the unperturbed system, with the exception of the K_p parameter for the subject-state 13SUC.

Though illuminating, this analysis is also limited. Given that each perturbation scheme was simulated only once per subject-state, a subject-state with few coherent data windows could have its parameter estimates exhibit significant deviations from the unperturbed values if the realization of the AWGN in any of its data windows is particularly noisy. Likewise, such a subject-state could observe very small deviations from the unperturbed values if the realization of the AWGN in any of its data windows is very quiet. Examining a distribution of estimated parameter values for each subject-state given a certain perturbation scheme would enhance this analysis, but would require performing parameter estimation on multiple realizations of each perturbation scheme, a rather time intensive task.

Missing from this analysis is perturbation of the SBP signal by standard noise patterns introduced by blood pressure monitoring equipment. Two common types of noise are a static offset or a slow drift (over the time scale of minutes) in the arterial blood pressure (ABP) waveform. A static offset in the ABP waveform results in a static offset in the SBP time series, which is then removed by the demeaning process in the parameter estimation and consequently does not alter any parameter estimates. A slow drift in the ABP waveform poses a more difficult challenge, but could likely be removed by some processing such as passing the ABP waveform through a high-pass or band-pass filter. Thus, neither of the standard sources of noise in blood pressure measurement should pose problems for the open-loop parameter estimation.

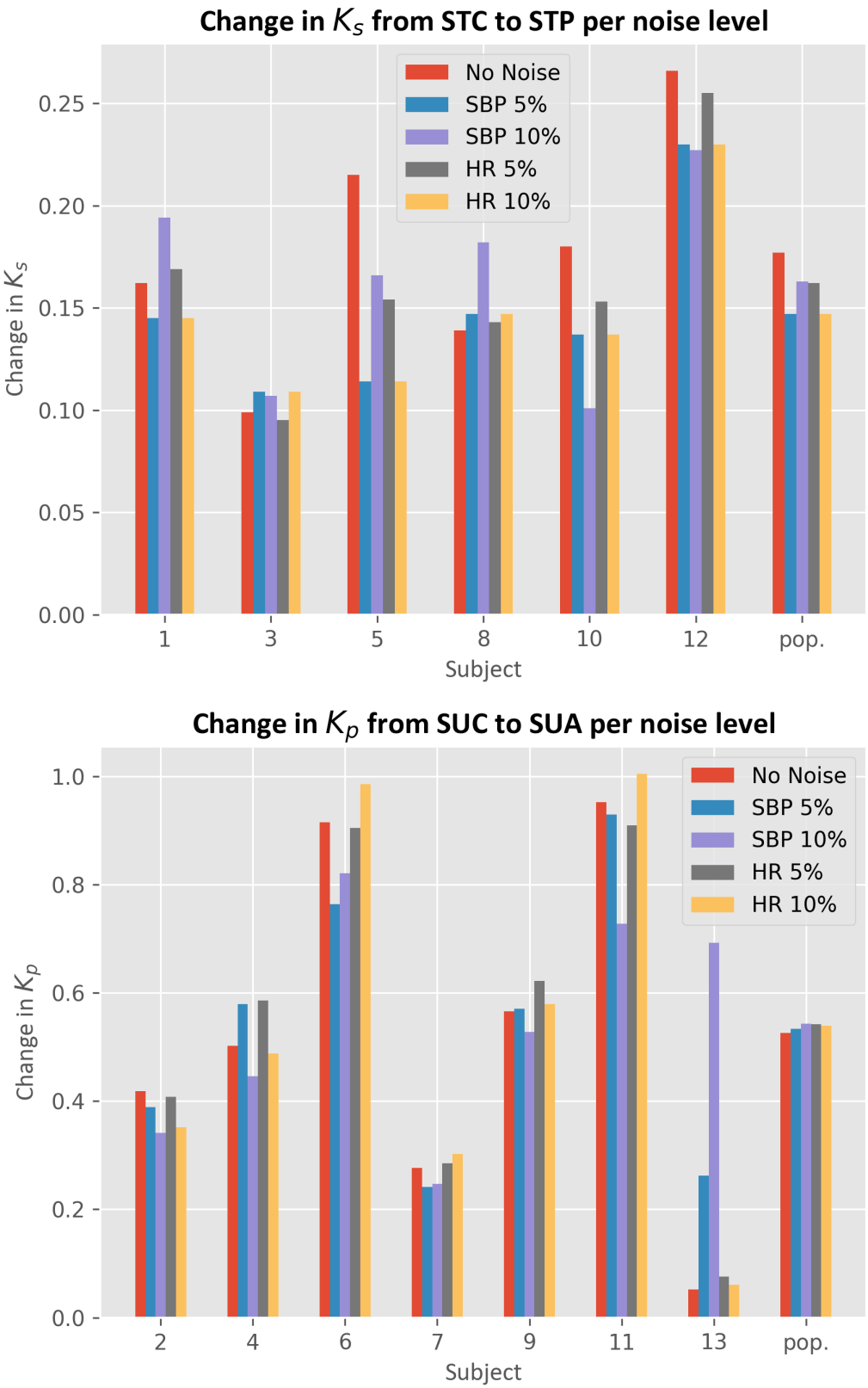

Figure 7.2: Changes in K_s from STC to STP for each perturbation scheme (top). Changes in K_p from SUC to SUA for each perturbation scheme (bottom). The subject "pop" represents population mean.

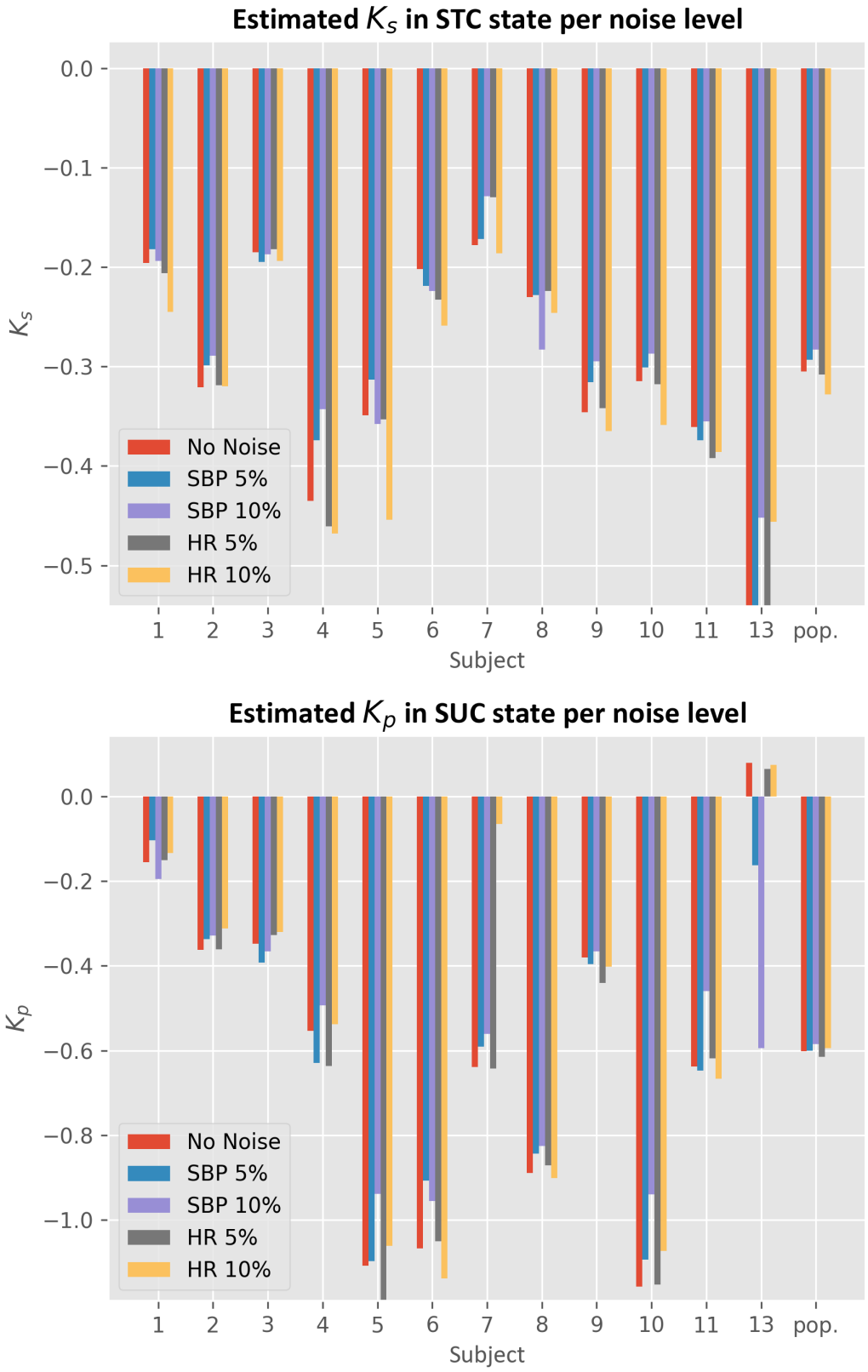

Figure 7.3: Estimated K_s in STC state for each perturbation scheme (top). Estimated K_p in SUC state for each perturbation scheme (bottom). The subject "pop" represents population mean.

Chapter 8

Conclusions

8.1 Contributions

The work in this thesis has contributed to the study of cardiovascular control and autonomic balance in two ways. First, we demonstrated that a low-order, open-loop model of baroreflex is able to track autonomic balance across a number of physiological states with varying degrees of autonomic activity and balance. Second, the lackluster performance of the closed-loop model in tracking autonomic balance demonstrated the limitations of models of baroreflex that only contain the heart rate control arc of blood pressure. These contributions may eventually lead to real-time tracking of the autonomic nervous system in a clinical setting.

8.2 Future Work

Three major areas for future exploration are data quantity, modeling, and data processing:

Data quantity: Given our dataset, we were able to demonstrate that the open-loop model is able to track changes in autonomic balance when the intervention effect is large, such as the change after pharmacological blockade of the SNS, the change after pharmacological blockade of the PNS, and the change after transitioning from the supine to standing posture. A dataset with more subjects and a finer sampling of physiological states along the axis of autonomic balance would provide a better evaluation of the model's sensitivity to changes in autonomic balance. Finer sampling of states could be achieved by recording data at varying levels of tilting, as opposed to the binary supine/standing regime. Similarly, different doses of the pharmacological agents could be administered to vary the level of sympathetic or parasympathetic blockade.

Modeling: Model error in the closed-loop model may most easily be reduced by adding in the contributions of the non heart rate arcs of the baroreflex. These contributions would be incorporated into the cardiovascular system block, and for example could include beat-to-beat values of total peripheral resistance (which can be extracted under suitable assumptions from the SBP signal using the Windkessel model) [7].

Data Processing: As mentioned in Chapter 4, respiratory contributions to heart rate variability will result in parameter values that are more positive than expected, particularly for the parasympathetic parameter. Removing these fluctuations from the

heart rate signal would likely improve the parameter estimates, and reduce parameter ensemble variability. This, however, requires developing a special filtering method for the heart rate time series because it is not uniformly spaced in the time domain.

Appendix A

We outline below our transfer function analysis methodology, beginning with signal extraction and ending with the computation of the baroreflex sensitivity (BRS). We also provide a table summarizing all of the BRS values computed using our implementation of the transfer function method.

Signal Extraction:

Given a subject-state, we assume that its ECG and ABP waveforms are time aligned (at least within the resolution of a beat). We then perform beat onset detection and extract the RRI beat series from the ECG recording employing the Pan-Topmkins algorithm [42]. Using the ABP waveform and the beat onsets, we next obtain the SBP beat series by finding the maximum pressure in the ABP waveform during each heartbeat. For both the RRI and SBP beat series, we generate a corresponding time series using a sample and hold. In the time series, each sample is held for the duration of a beat, *i.e.* it is held for the corresponding R-R interval. For example, suppose we had (2, 5, 3) and (88, 84, 80) as our RRI and and SBP beat series respectively, where for convenience we measure RRI in units of *samples*, then their respective time series would be (2, 2, 5, 5, 5, 5, 5, 3, 3, 3) and (88, 88, 84, 84, 84, 84, 84, 80, 80, 80). Lastly, we decimate the RRI and SBP time series to 2Hz signals that we will label as RRI_d and SBP_d

BRS Computation:

Using Welch's method with a window size of 256 samples, an overlap of 128 samples, and Hamming windowing, we compute the auto-spectra of both RRI_d and SBP_d, as well as the cross-spectrum between RRI_d and SBP_d [43]. We obtain the coherence between RRI_d and SBP_d by taking the per frequency quotient of the magnitude of the cross-spectrum squared by the product of the RRI_d and SBP_d auto-spectra. We next compute the transfer function from SBP_d to RRI_d by taking the per frequency quotient of the cross spectrum by the auto-spectrum of SBP_d. Finally, we estimate BRS as the magnitude of the transfer function at the frequency in the LF band (0.04-0.15Hz) with greatest coherence. All of the computations beginning with the coherence are expressed mathematically below.

$$\mathrm{RRI}_d\ Autospectra := S_{RR}\left(f\right)$$

$$\mathrm{SBP}_d\ Autospectra := S_{BB}\left(f\right)$$

$$Cross\ Spectrum := S_{BR}(f)$$

$$Coherence := \gamma^2\left(f\right) = \frac{\left|S_{BR}(f)\right|^2}{S_{BB}\left(f\right) * S_{RR}(f)}$$

$$Transfer\ Function := H\left(f\right) = \frac{S_{BR}(f)}{S_{BB}\left(f\right)}$$

$$f^* = argmax\ \gamma^2\left(f\right) \quad for \quad f\ \epsilon\ \left(0.05, 15\right)$$

$$BRS = \left|H(f^*)\right|$$

Propranolol First	Subject	01	03	05	08	10	12	
ST	B	1.89	N/A	0.94	5.02	0.91	0.93	
	C	9.53	6.73	31.73	12.59	11	10.57	
	P	9.39	13.63	32.15	15.99	10.32	12.96	
SU	B	1.64	5.76	1.01	4.23	0.64	1.6	
	C	17.24	22.92	45.61	16.78	30.9	30.74	
	P	17.77	50.28	49.83	15.83	30.96	38.69	
Atropine First	Subject	02	04	06	07	09	11	13
ST	A	0.96	1.62	1.9	0.56	1.55	1.05	0.82
	B	2.42	2.53	2.04	1.53	1.56	2.96	3.21
	C	7.09	8.27	16.41	10.45	8.27	6.41	10.44
SU	A	6.78	0.99	1.47	12.39	2.03	2.07	0.69
	B	5.59	4.64	5.68	1.04	1.87	4.5	1.28
	C	11.53	21.92	42.59	21.61	17	14.13	20.99

Table A.1: BRS values obtained for each subject-state using our implementation of the transfer function method. To find a subject state, first look for the column corresponding to the subject, and then find the row corresponding to the three-letter state.

Bibliography

[1] Texas Heart Institute. (August 2016). *Heart Anatomy* [Online]. Available: http://www.texasheart.org/HIC/Anatomy/anatomy2.cfm

[2] R.G. Mark (2004) *Introduction: The Functional Anatomy of the Cardiovascular System* [Online]. Available: https://ocw.mit.edu/courses/health-sciences-and-technology/hst-542j-quantitative-physiology-organ-transport-systems-spring-2004/readings/function_anatomy.pdf

[3] L.S. Costanzo, *Physiology*, Philadelphia, PA: Saunders/Elsevier, 2013.

[4] R.G. Mark (2004) *Principles of Cardiac Electrophysiology* [Online]. Available: https://ocw.mit.edu/courses/health-sciences-and-technology/hst-542j-quantitative-physiology-organ-transport-systems-spring-2004/readings/car_elec_phy.pdf

[5] R.G. Mark (2004) *Clinical Electrocardiography and Arrythmias* [Online]. Available: https://ocw.mit.edu/courses/health-sciences-and-technology/hst-542j-quantitative-physiology-organ-transport-systems-spring-2004/readings/clin_elec_card.pdf

[6] R.G. Mark (2004) *Control and Integration in the Cardiovascular System* [Online]. Available: https://ocw.mit.edu/courses/health-sciences-and-technology/hst-542j-quantitative-physiology-organ-transport-systems-spring-2004/readings/cont_and_intg.pdf

[7] R.G. Mark (2004) *Cardiovascular Mechanics* [Online]. Available: https://ocw.mit.edu/courses/health-sciences-and-technology/hst-542j-quantitative-physiology-organ-transport-systems-spring-2004/readings/cardio_mech.pdf

[8] A.C Guyton, J.E. Hall, *Textbook of Medical Physiology*. 11th ed. Philadelphia, PA: Saunders/Elsevier, 2006.

[9] S. Akselrod, D. Gordon, F.A. Ubel, D.C. Shannon, A.C. Berger, R.J. Cohen, "Power spectrum analysis of heart rate fluctuation: a quantitative probe of beat-to-beat cardiovascular control," *Science*, vol. 213, no. 4504, pp. 220-222, 1981.

[10] S. Akselrod, D. Gordon, J.B. Madwed, N.C. Snidman, D.C. Shannon, R.J. Cohen, "Hemodynamic regulation: investigation by spectral analysis," *Am. J. Physiol.*, vol. 249, no. 4, pp. H867-H875, 1985.

[11] Task Force of the European Society of Cardiology and the North American Society of Pacing Electrophysiology, "Heart rate variability: standards of measurement, physiological interpretation, and clinical use." *Circulation*, vol. 93, no.5, pp. 1043-1065, 1996.

[12] C. Julien, "The enigma of Mayer waves: facts and models," *Cardiovasc. Res.*, vol. 70, no. 1, pp. 12-21, 2006.

[13] P.K. Stein, M.S. Bosner, R.E. Kleiger, B.M. Conger, "Heart rate variability: a measure of cardiac autonomic tone," *Am. Heart J.*, vol. 127, no. 5, pp. 1376-1381, 1994.

[14] M. Pagani, F. Lombardi, S. Guzzetti, O. Rimoldi, R. Furlan, P. Pizzinelli, *et al.*, "Power spectral analysis of heart rate and arterial pressure variabilities as a marker of sympatho-vagal interaction in man and conscious dog," *Circ. Res.*, vol. 59, no. 2, pp. 178-193, 1986.

[15] D.L. Eckberg, "Sympathovagal balance: a critical appraisal," *Circulation*, vol. 96, no. 4, pp. 3224-3232, 1997.

[16] C. M. Brown, "Experimental Studies of the Baroreflex," in *Mathematical Modeling and Validation in Physiology: Applications to the Cardiovascular and Respiratory Systems*. J. J. Batzel, M. Bachar, and F. Kappel, Eds. Heidelberg, Germany: Springer, 2013.

[17] H.W. Ead, J. H. Green, E. Neil, "A comparison of the effects of pulsatile and non-pulsatile blood flow through the carotid sinus on the reflexogenic activity of the sinus baroreceptors in the cat," *J. Physiol.,* vol. 118, no. 4, pp. 509-519, 1952.

[18] J.R. Levick, "Cardiovascular receptors, reflexes and central control," in *An Introduction to Cardiovascular Physiology.* 5th ed. London, United Kingdom: Hodder Arnold, 2010.

[19] H.M. Stauss, "Baroreceptor reflex function," *Am. J. Physiol.,* vol. 283, no. 2, pp. R284-R286, 2002.

[20] A.V. Oppenheim, G.C. Verghese, *Signals, Systems and Inference*. Boston, MA: Pearson, 2015.

[21] G. Bertinieri, M. Di Rienzo, A Cavallazzi, A.U. Ferrari, A Pedotti, G. Mancia, "Evaluation of baroreceptor reflex by blood pressure monitoring in unanesthetized cats," *Am. J. Physiol.,* vol. 254, no.2, pp. H377-H383, 1988.

[22] M. Di Rienzo, G. Bertinieri, G Mancia, A Pedotti, "A new method for evaluating the baroreflex role by a joint pattern analysis of pulse interval and systolic blood pressure series," *Med. Bio. Eng. Comput.* vol. *23*, pp. 313-314, 1985.

[23] C.A. Swenne, "Baroreflex sensitivity: mechanisms and measurements," *Neth. Heart J.*, vol. 21, pp. 58-60, 2013.

[24] G. Parati, M. Di Rienzo, G. Mancia, "Dynamic modulation of baroreflex sensitivity in health and disease," *Ann. NY. Acad. Sci.*, vol. 940, pp. 469-487, 2001.

[25] R.W. deBoer, J.M. Karemaker, and J. Strackee, "Relationships between short-term blood-pressure fluctuations and heart-rate variability in resting subjects I: a spectral analysis approach," *Med. & Biol. Eng. & Comput.*, vol. 23, no. 4, pp. 352-358, 1985.

[26] H.W. Robbe, L.J. Mulder, H. Ruddel, W.A. Langewitz, J.B. Veldman, and G Mulder, "Assessment of baroreceptor reflex sensitivity by means of spectral analysis," *Hypertension,* vol. 10, no. 5, pp. *538-543*, 1987.

[27] X. Chen, R. Mukkamala, "Selective quantification of the cardiac sympathetic and parasympathetic nervous systems by multisignal analysis of cardiorespiratory variability," *Am. J. Physiol.,* vol. 294, no. 1, pp. H362-H371, 2008.

[28] R.D. Berger, J.P. Saul, R.J. Cohen, "Transfer function analysis of autonomic regulation. I. Canine atrial rate response," *Am. J. Physiol.,* vol. 256, no. 1, pp. H142-H152, 1989.

[29] T.J. Mullen, M.L. Appel, R. Mukkamala, J.M. Mathias, R.J. Cohen, "System identification of closed-loop cardiovascular control: effects of posture on autonomic blockade," *Am. J. Physiol.,* vol. 272, no. 1, pp. H448-H461, 1997.

[30] V. Chirravuri, "Identifying a Low-Order Beat-to-Beat Model of Arterial Baroreflex," M.Eng Thesis, Dept. of EECS, MIT, Cambridge, Massachusetts, 2010

[31] R.W. deBoer, J.M. Karemaker, and J. Strackee, "Comparing spectra of a series of points events particularly for heart rate variability data," *IEEE Trans. Biomed. Eng.,* vol. 31, no. 4, pp. 384-387, 1984.

[32] J.P. Saul, R.D. Berger, P. Albrecht, S.P. Stein, M.H. Chen, R.J. Cohen, "Transfer function analysis of circulation: unique insights into cardiovascular regulation." *Am. J. Physiol.,* vol. 261, no. 4, pp. H1231-H1245, 1991.

[33] J.P. Saul, R.D. Berger, M.H. Chen, R.J. Cohen, "Transfer function analysis of autonomic regulation. II. Respiratory sinus arrhythmia," *Am. J. Physiol.,* vol. 256, no. 25, pp. H153-H161, 1989.

[34] X. Xiao, "Principal Component Based System Identification and its Applications to the Study of Cardiovascular Regulation," Ph.D Thesis, Dept. of HST, MIT, Cambridge, Massachusetts, 2004

[35] D.J. Wales, J.P.K. Doye, "Global Optimization by Basin-Hopping and the Lowest Energy Structures of Lennard-Jones Clusters Containing up to 110 Atoms," *J. Phys. Chem.,* vol. 101, no. 28, pp. 5111-5116, 1997.

[36] D.J. Wales, H.A. Scheraga, "Global Optimization of Clusters, Crystals, and Biomolecules," *Science,* vol. 285, pp. 1368-1372, 1999.

[37] X. Chen, R. Mukkamala, "Selective quantification of the cardiac sympathetic and parasympathetic nervous systems by multisignal analysis of cardiorespiratory variability," *Am. J. Physiol.,* vol. 294, no. 1, pp. H362-H371, 2008.

[38] M.L. Appel, "Closed Loop Identification of Cardiovascular Regulatory Mechanisms," Harvard Univ, Cambridge, Massachusetts, 1992

[39] D. Eckberg, "Temporal response patterns of the human sinus node to brief carotid baroreceptor stimuli," *J. Physiol.,* vol. 258, no. 3, pp. 769-782, 1976.

[40] R.D. Berger, "Analysis of the Cardiovascular Control System Using Broad Band-Stimulation," Ph.D Thesis, Dept. of EECS, MIT, Cambridge, Massachusetts, 1987.

[41] A.V. Oppenheim, G.C. Verghese, *Signals, Systems and Inference*. Boston, MA: Pearson, 2015.

[42] J. Pan, W.J. Tompkins, "A real-time QRS detection algorithm" *IEEE Trans. Biomed. Eng.*, vol.32, no. 3, pp. 230-236, 1985.

[43] P.D. Welch, "The use of fast Fourier transform for the estimation of power spectra: A method based on time averaging over short, modified periodograms," *IEEE Trans. Audio Electroacoust.*, vol. 15, no. 2, pp. 70-73, 1967.